ACS Energy LETTERS

http://pubs.acs.org/journal/aelccp

Methylammonium Triiodide for Defect Engineering of High-Efficiency Perovskite Solar Cells

Essa A. Alharbi, Anurag Krishna, Thomas P. Baumeler, Mathias Dankl, George C. Fish, Felix Eickemeyer, Olivier Ouellette, Paramvir Ahlawat, Viktor Škorjanc, Elsa John, Bowen Yang, Lukas Pfeifer, Claudia Esther Avalos, Linfeng Pan, Mounir Mensi, Pascal Alexander Schouwink, Jacques-E. Moser, Anders Hagfeldt, Ursula Rothlisberger, Shaik M. Zakeeruddin, and Michael Grätzel*

Cite This: *ACS Energy Lett.* 2021, 6, 3650−3660

Read Online

ACCESS | Metrics & More | Article Recommendations | Supporting Information

ABSTRACT: **The defects present in metal halide perovskite are deleterious to both the performance and stability of photovoltaic devices. Consequently, there is an intense focus on developing defect mitigation strategies. Herein we report a facile strategy that employs methylammonium triiodide (MAI_3) as an additive to the perovskite precursor solution. We examine the effect of MAI_3 on the structural and optoelectronic properties by X-ray diffraction, density functional theory calculations, molecular dynamics simulations, solid-state nuclear magnetic resonance, steady-state, time-resolved photoluminescence (TRPL), and time-resolved terahertz spectroscopy (TRTS). Specifically, TRPL and TRTS show that MAI_3 suppresses nonradiative recombination and increases the charge carrier mobility. As a result, the champion device shows a power conversion efficiency (PCE) of 23.46% with a high fill factor of >80%. Furthermore, these devices exhibit enhanced operational stability, with the best device retaining ∼90% of its initial PCE under 1 sun illumination with maximum power point tracking for 350 h.**

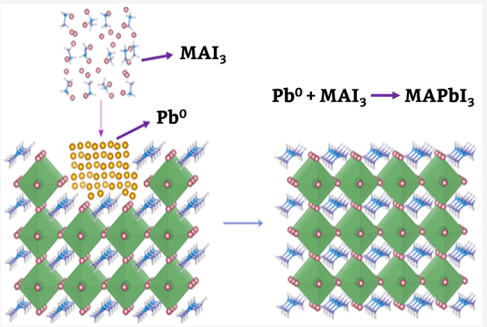

Metal halide perovskites have emerged as one of the most attractive light-harvesting materials for next-generation solar cells. Within a decade of the first report, the certified power conversion efficiency (PCE) of perovskite solar cells (PSCs) has reached as high as 25.5%.[1−4] However, before bringing PSCs to an industrial scale-up process and using perovskites in other optoelectronic applications, some critical issues need to be carefully addressed, such as Pb and solvent toxicities and, most importantly, the intrinsic material and device instability. Lattice defects have been identified as one of the main sources of instability and performance loss via charge recombination through nonradiative channels.[5,6] Perovskite crystals, in particular, $FAPbI_3$, contain several types of point defects such as interstitials (FA_i, Pb_i, I_i), vacancies (V_{FA}, V_{Pb}, V_I), antisites (FA_{Pb}, Pb_{FA}, FA_I, Pb_I, I_{FA}, I_{Pb}), grain boundaries, and mobile ions, which have been identified as predominant sources for nonradiative recombination.[7] Most of these point defects result only in shallow traps or tail states; however, the ionic nature of hybrid perovskites leads to a large population of mobile ions. The vacancies, in particular, iodide vacancies, provide a diffusion pathway for halide ions. In particular, iodide migrates to perovskite interfaces under an electric field, thus compromising the photovoltaic performance and long-term operational stability. Apart from point defects, perovskite crystals also contain undercoordinated Pb^{2+} and lattice I^- ions susceptible to reduction and oxidation (redox) reactions, respectively.[8] The reduction of undercoordinated Pb^{2+} leads to metallic Pb (Pb^0), which critically acts as a center for nonradiative recombination and a source of degradation. Lattice I^- ions can be oxidized by hole trapping to interstitial I^0, which can cause irreversible decomposition of the perovskite by dimerizing to volatile I_2, triggering the perovskite degradation.[9] Therefore, it is imperative to suppress these deleterious reaction channels. The ionic nature of the perovskite lattice allows for the molecular passivation of these defects. Various strategies, such as compositional

Received: August 19, 2021
Accepted: September 20, 2021

https://doi.org/10.1021/acsenergylett.1c01754
ACS Energy Lett. 2021, 6, 3650−3660

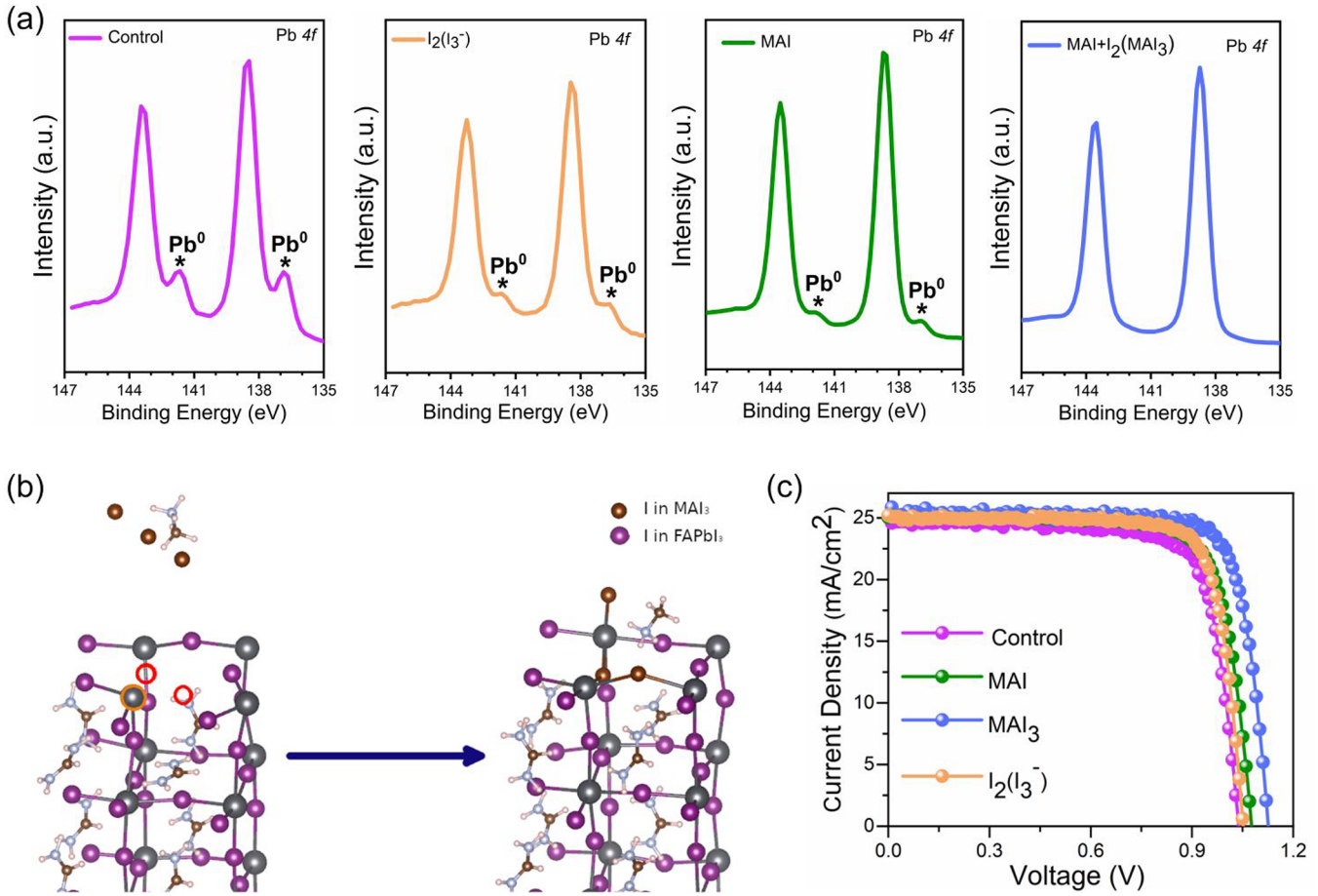

Figure 1. (a) High-resolution XPS spectra of Pb 4f with and without additives. (b) Gas-phase-optimized initial and final states for the addition reaction of MAI_3 onto a $FAPbI_3$ surface with two halide vacancy defects (red circles) located next to Pb^0 (orange circle). (c) J–V curves of the devices with and without additives.

engineering,[10−13] iodine management, 2D/3D perovskite heterostructures,[14,15] bulk and surface/interface passivation via small organic molecules,[16−18] ammonium salts,[19] and ionic additives[20] have been used for defect mitigation. Nevertheless, there are ongoing efforts to develop facile defect passivation strategies and to improve our fundamental understanding of the mechanisms involved.

Herein we investigate methylammonium triiodide (MAI_3) as an additive for holistic defect mitigation in a perovskite semiconductor. MAI_3 has a low melting point, a large dipole moment, and a cation bearing an ammonium headgroup, which allows it to form numerous H bonds, ensuring strong interactions with anions and neutralizing charged vacancies.[21] Our results show that MAI_3 passivates deleterious Pb^0 defects. As a result, PSCs treated with MAI_3 exhibit reduced nonradiative recombination and an improved charge transport, leading to stabilized PCEs of >23% with a high fill factor (FF) of >80% and improved device stability under different stress conditions.

We employ a perovskite with a $FAPbI_3$-rich composition of $(FAPbI_3)_{0.98}(MAPbBr_3)_{0.02}$ (FA^+ = formamidinium = $CH(NH_2)_2^+$; MA^+ = methylammonium = $CH_3NH_3^+$). The additives were added to the perovskite precursor solution, and perovskite films were deposited by spin-coating onto the mesoporous TiO_2 (mp-TiO_2) layer by a one-step method using chlorobenzene as an antisolvent. To begin with, we prepared the additive solutions of I_2, MAI, and MAI+I_2 by dissolving them in isopropyl alcohol (IPA) at 70 °C. We recorded the absorption spectra as a function of time (Figure S1a−c). In the case of the mixture of MAI and I_2, we observed two absorption bands at 291 and 358 nm immediately after the preparation, which corresponds to I_3^-,[22] thus confirming the formation of MAI_3. Furthermore, these absorption bands did not change with time, and no other bands appeared, as shown in Figure S1a−c. In the case of iodine (I_2) dissolved in IPA, we observe the formation of triiodide, as confirmed by weak absorption bands at 291 and 358 nm and an additional absorption peak related to I_2 at 443 nm. After 72 and 220 h, the formation of I_3^- became clearer; however, the absorption band relating to I_2 at 443 nm was still observed (Figure S1a−c). Thus it is evident that a mixture of MAI+I_2 in IPA leads to the formation of a stable MAI_3 solution, whereas I_2 in IPA results in a mixture of I_3^- and I_2. Typically, because of the soft nature of the perovskite material, in particular, the weak bond of Pb−I, metallic lead (Pb^0) and iodine (I^0) can be easily formed, which are known to be sources of recombination and degradation.[8] We hypothesize that MAI_3 can stop the formation of Pb^0 and therefore reduce this degradation. To verify our hypothesis, we performed X-ray photoelectron spectroscopy (XPS) of a pristine perovskite and with the additives of $I_2(I_3^-)$, MAI, and MAI+I_2(MAI_3). We observed the formation of Pb^0 in the pristine perovskite (control) and the perovskite with MAI and I^-_3 as additives, whereas there was no presence of Pb^0 in the perovskite with MAI_3, as shown

https://doi.org/10.1021/acsenergylett.1c01754
ACS Energy Lett. 2021, 6, 3650−3660

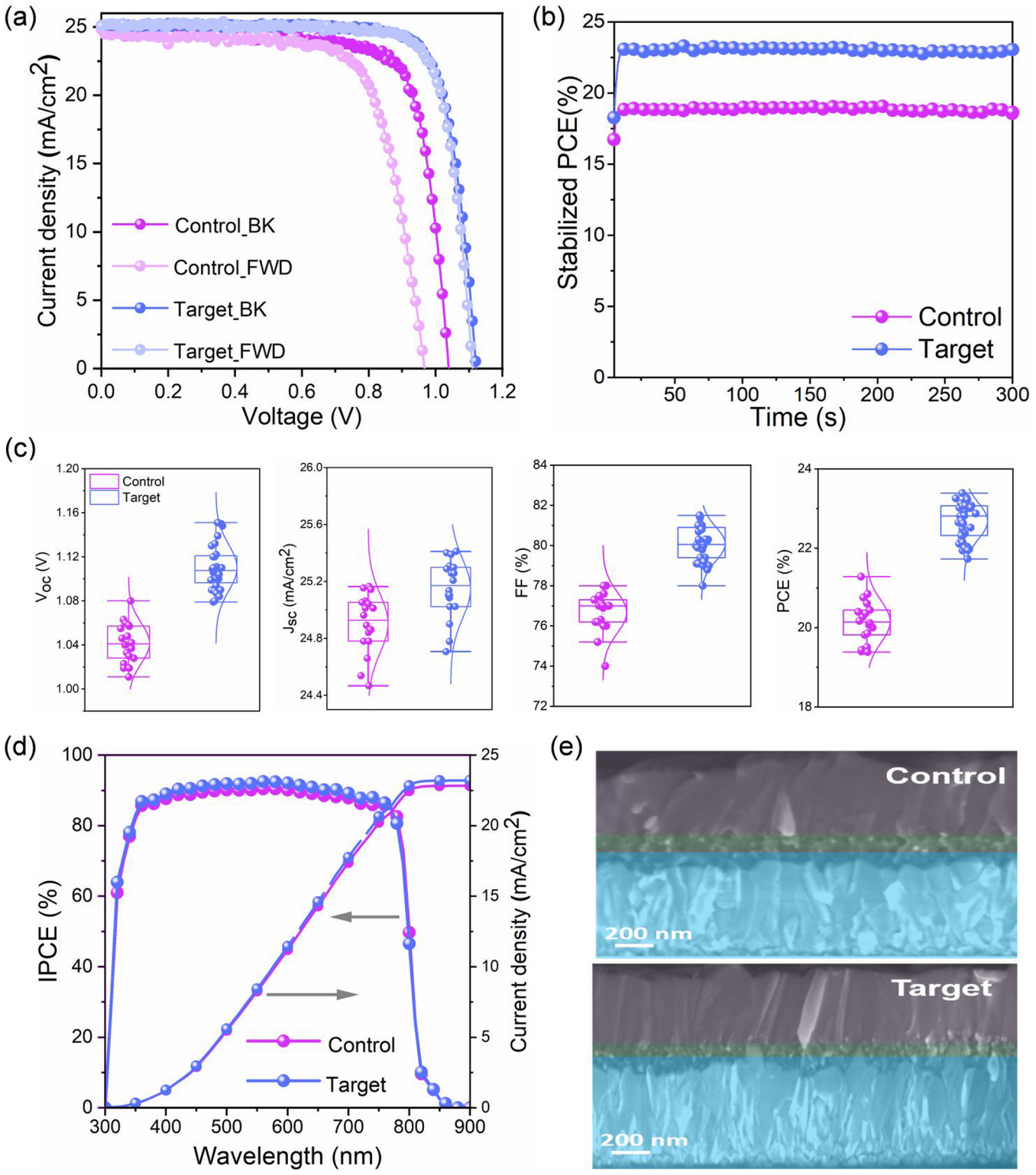

Figure 2. (a) *J*–*V* curves of the devices at backward and forward scan. (b) Maximum power point tracking for Control and Target. (c) Statistical distribution *J*–*V* parameters of Control and Target devices. (d) IPCE spectra and photocurrent integrated over the standard AM 1.5G solar spectrum. (e) Cross-sectional SEM images of Control and Target devices, respectively.

in Figure 1a–c. This confirms that the MAI_3 additive completely reacted with the Pb^0, which is a well-known source of nonradiative recombination and degradation. To further verify our hypothesis, we performed density functional theory (DFT) calculations to investigate possible reactions occurring when MAI_3 approaches a slab of $FAPbI_3$ containing a cluster of three surface defects, namely, two halide vacancies sharing a common neighboring metallic Pb. Formally, such a Pb has an oxidation state of 0 serving as a suitable starting point for a formal redox reaction of the kind

$$Pb^0 + MA^+(I_3)^- \rightarrow MA^+Pb^{2+}(I^-)_3$$

https://doi.org/10.1021/acsenergylett.1c01754
ACS Energy Lett. 2021, 6, 3650–3660

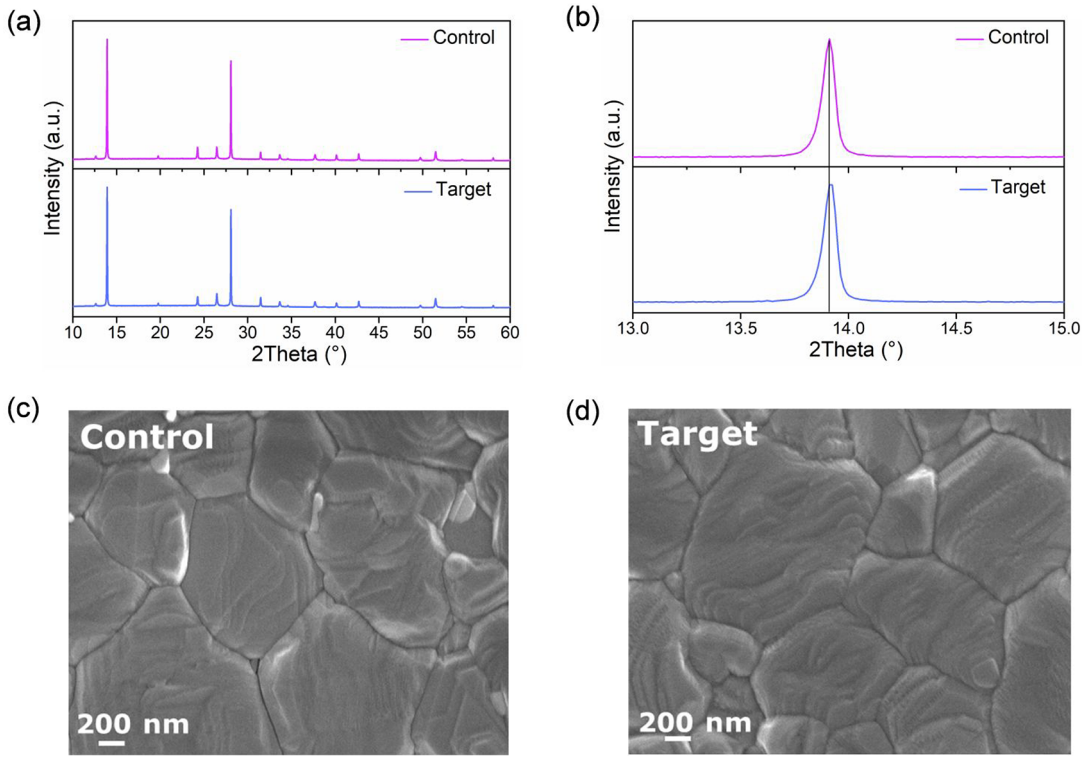

Figure 3. (a,b) XRD patterns and (c,d) top-view SEM images of Control and Target films.

A simple energetic estimate (Supporting Information (SI)) based on the involved ionization energies, electron affinities, and dissociation energies with respect to the lattice energy predicts that such a reaction is highly exothermic.

In fact, we find that when the MAI_3 approaches the surface from different starting configurations within a distance of 3.0 to 3.5 Å to the halide vacancies, it invariably dissociates with the simultaneous incorporation of iodides into the vacant anion sites and a third I^- coordinating to an undercoordinated Pb ion at the surface (Figure 1b). In the gas phase, this process is calculated to be exothermic by about −5 eV per stoichiometric unit. To assess the underlying redox character, we computed Bader charges on reactants and products (SI), demonstrating that a significant transfer of electronic charge from the Pb atoms of the surface to the I_3^- indeed occurs. Therefore, we conclude that MAI_3 can be fully converted to perovskite with the simultaneous elimination of notorious Pb^0 defects and iodide and MA^+ vacancies. We carried out a systematic investigation of the effect of these additives (MAI_3, MAI, and I_3^-) (see the Experimental Methods for more information) on the photovoltaic performance. We fabricated solar cells with an n−i−p architecture. The champion device using (I_2) I_3^- showed a PCE of 21.43% with a J_{SC} of 25.20 mA·cm^{-2}, a V_{oc} of 1.05 V, and an FF of 79.5%, and while using MAI as an additive, it produced a PCE of 21.08% with a J_{SC} of 25.03 mA·cm^{-2}, a V_{oc} of 1.08 V, and an FF of 77.0%. In contrast, the MAI_3 showed a dramatic improvement with a champion PCE of 23.46%, a J_{SC} of 25.20 mA·cm^{-2}, and a clear improvement in the V_{oc} and FF to 1.13 V and 81.4%, respectively. In comparison, the control device showed a PCE of 20.32% with a J_{SC} of 25.06 mA·cm^{-2}, a V_{oc} of 1.04 V, and an FF of 76.7%, as shown in Figure1c. The photovoltaic results and data are shown and summarized in Figure S2a−c and Table S1.

After screening the additives, we could see that the best results were obtained with MAI_3. From here on, we performed an in-depth investigation of the impact of the MAI_3 additive using multicharacterization techniques to unravel its effect on the device photophysics and determine the impact of the device stability. Hereafter, the pristine perovskite is referred to as the Control, and perovskite with 5 and 10 mM of MAI_3 is referred to as the Target and Target-ex, respectively. We performed backward and forward scans to examine the hysteresis in the Control and Target devices (Figure 2a). The Control device showed a PCE of 19.77% in the backward scan and 17.28% in the forward scan, whereas the Target showed a PCE of 23.10% in the backward scan and 22.67% in the forward scan, which translated to a hysteresis index (HI = $[(PCE_{backward} - PCE_{forward})/(PCE_{backward})] \times 100$ of 12.60 and 1.86% for the Control and Target devices, respectively. Figure 2b shows the stabilized power output (SPO) for the best-performing devices during maximum power point (MPP) tracking in ambient air (15−25% RH (relative humidity)) under 1 sun illumination for 300 s. The SPO upon MPP tracking for the Control and Target is 18.55 and 22.97%, respectively. The statistical distribution of the photovoltaic characteristics (J_{SC}, V_{OC}, FF, and PCE) is presented in Figure 2c, which shows an improvement in all device parameters. Furthermore, the incident photon-to-current efficiency (IPCE) spectra and integrated current density (Figure 2d) of the target device show almost no change in the onset of the IPCE spectra and the inflection point (Figure S4) as compared with the Control, which shows a band gap of 1.555 eV. The cross-section morphologies of the Control and Target PSCs (Figure 2e) were characterized by scanning electron microscopy (SEM). The cross-sectional SEM images showed a well-stacked perovskite layer thickness of ∼500 nm.

https://doi.org/10.1021/acsenergylett.1c01754
ACS Energy Lett. 2021, 6, 3650−3660

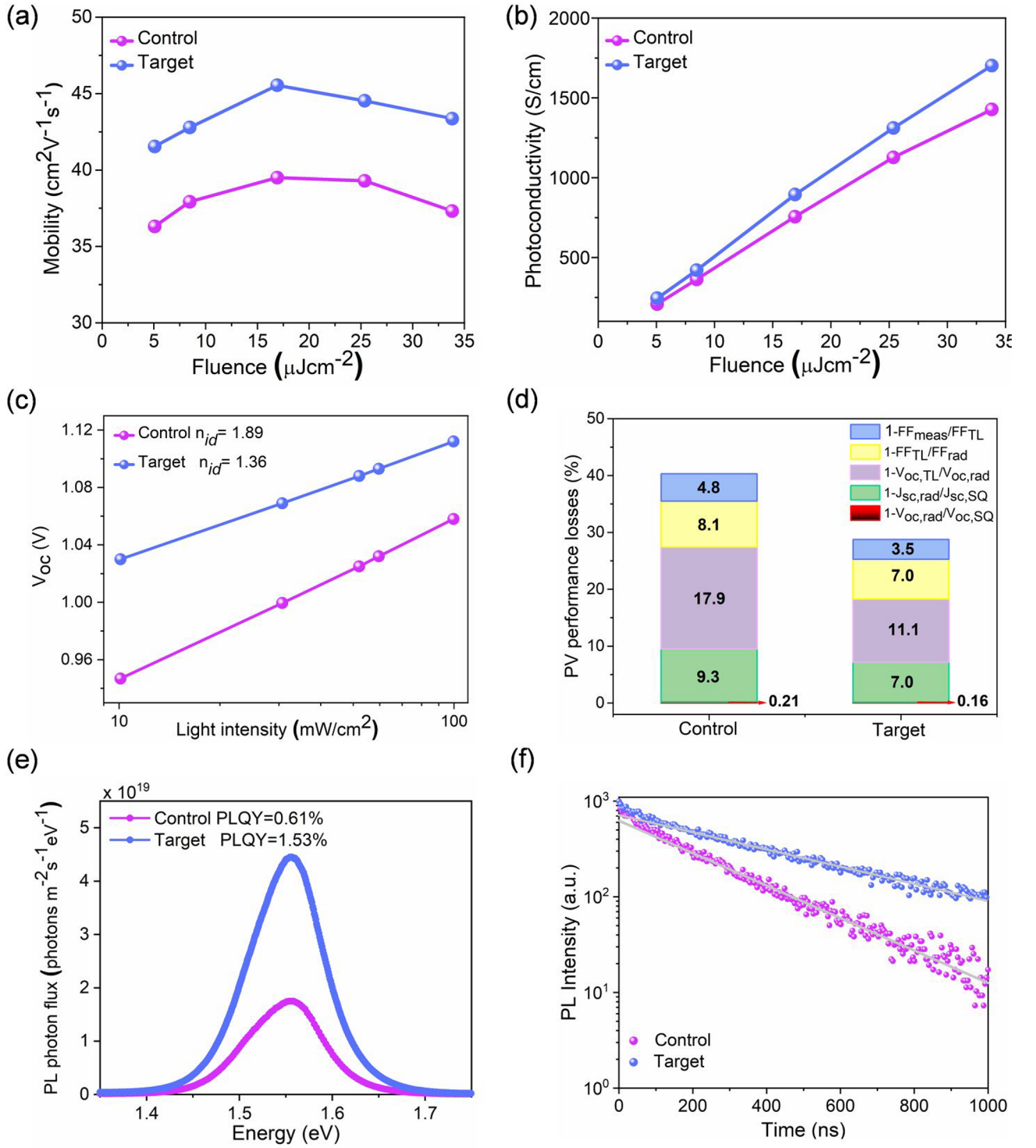

Figure 4. (a,b) THz carrier mobility and material photoconductivity as a function of pulsed excitation energy fluence at λ = 580 nm. (c) Open-circuit voltage (V_{oc}) at a different light intensities. (d) PV performance loss evolution. (e) Absolute photon flux measurements of complete devices at 1 sun excitation from which the PLQY is determined. (f) Time-resolved photoluminescence (TRPL) measurements of Control and Target, respectively.

The crystallinity and structural properties of perovskite films were analyzed by X-ray diffraction (XRD) (Figure 3a,b and Figure S5a,b). We found that the presence of a PbI_2 peak at 12.5° remained in all films, which originated from the use of a 3% excess of PbI_2 in the perovskite precursor solution. Upon the addition of 5 (Target) and 10 mM (Target-ex) MAI_3 into the Control perovskite ($(FAPbI_3)_{0.98}$ $(MAPbBr_3)_{0.02}$), we observed that the incorporation of MA^+ was successfully integrated into the crystal lattice of $FAPbI_3$ via a clear shift to a higher angle, as shown in Figure 3a and Figure S5b. Also, we calculated the lattice cell parameters with and without the addition of MAI_3, and it was found that the structure was tetragonal with (a = 8.9655 Å, c = 12.6891 Å), (a = 8.9608 Å, c = 12.6872 Å), and (a = 8.9596 Å, c = 12.6866 Å) for the

https://doi.org/10.1021/acsenergylett.1c01754
ACS Energy Lett. 2021, 6, 3650−3660

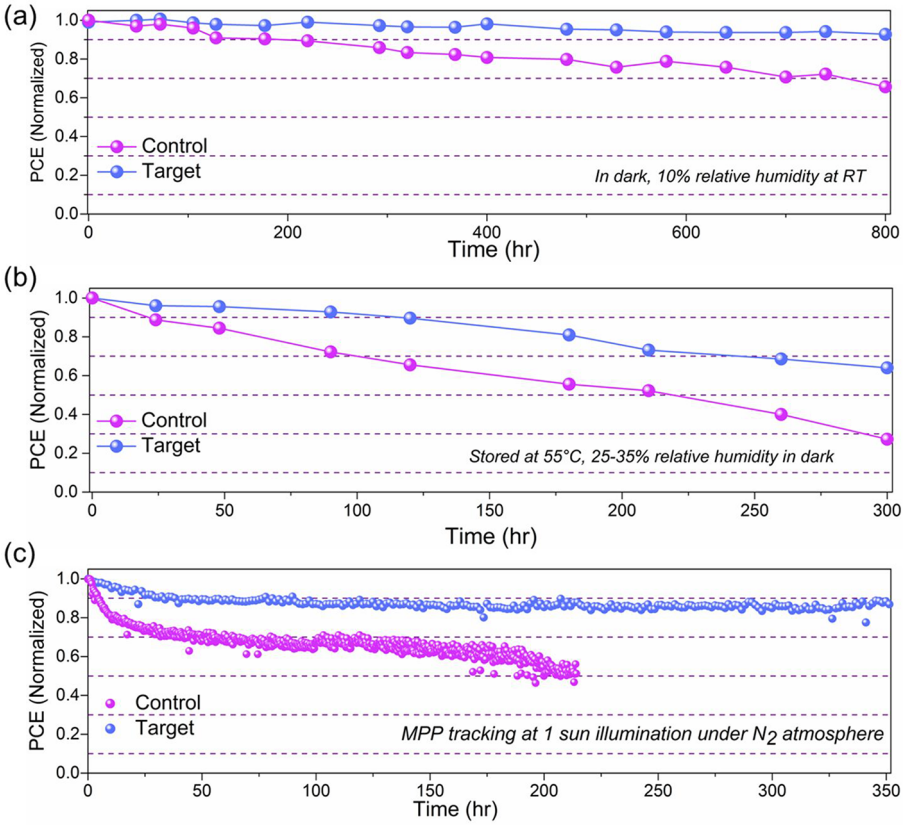

Figure 5. Long-term stability. (a) Shelf life at room temperature (RT), in the dark with 10% relative humidity. (b) Devices were stored at 55 °C with a relative humidity of ∼25−35% in the dark. (c) Operational stability in a nitrogen environment at room temperature under continuous illumination (white LED, 1 sun) at maximum power point for Control and Target, respectively.

Control, Target, and Target-ex, respectively. To quantify the incorporation of MA^+ into the lattice of $FAPbI_3$, we used solid-state nuclear magnetic resonance (ssNMR), as shown in Figure S6. From ssNMR, we quantified that the Control film had only 1.3% of MA^+, whereas the Target and Target-ex contained 3.2 and 3.8% of MA^+, respectively, which confirmed the incorporation of MA^+ in the lattice, as suggested by XRD. Furthermore, this allowed the compositions to be redefined as Control $(FAPbI_3)_{0.987}$ $(MAPbBr_3)_{0.013}$, Target $(FAPbI_3)_{0.986}$ $(MAPbBr_3)_{0.032}$, and Target-ex $(FAPbI_3)_{0.962}$ $(MAPbBr_3)_{0.038}$. We further performed MD simulations to check the impact of the MAI_3 on the phase stability of cubic $FAPbI_3$. We performed qualitative energy barrier calculations between cubic-$FAPbI_3$ and delta-$FAPbI_3$ for three cases: (a) without any iodide vacancy, (b) having three iodide vacancies (out of 72 iodine atoms in a 288-atom supercell), and (c) having six iodide vacancies. For these calculations, we used classical molecular dynamics (MD) simulations,[23,24] the computational details of which are discussed in the Experimental Methods section. We found a systematic decrease in the energy barrier from the cubic to the delta phase with an increasing number of iodide vacancies, as shown in Figure S5c. This behavior shows that iodide vacancies in bulk might also act as nucleation centers for the formation of delta-$FAPbI_3$, providing a further rationalization for the observed substantial increase in the stability of the Target as compared with the control sample. The surface morphology in the SEM images (Figure 3c,d) shows that both Control and Target perovskite films are uniform and highly crystalline with similar compact textures and grain sizes of hundreds of nanometers.

Next, we carried out an in-depth investigation of the optoelectronic properties of the Control and Target films. We performed time-resolved terahertz spectroscopy (TRTS) to get insights into the intrinsic charge carrier mobility and conductivity. The spectra and kinetics are shown in Figures S7 and S8, respectively. The spectra for both the Control and Target are predominantly flat, and so we can conclude that there is no phase shift taking place, which can lead to artifacts in the kinetic measurements. We can clearly see that the mobility (Figure 4a) and photoconductivity (Figure 4b) improved upon the addition of MAI_3 as compared with the Control film at different fluences. This enhancement of mobility and photoconductivity could be one of the factors for the increase in the FF in the Target devices. To further verify this, we analyzed the devices in terms of the diode characteristics. In Figure 4c, we measured the ideality factor (n_{id}) by taking the dependence of V_{OC} as a function of the incident light intensity. Upon the addition of 5 mM of MAI^-_3 (Target), the n_{id} decreased from 1.89 to 1.36, which indicates a substantial reduction in the nonradiative recombination. Then, we fitted the $J-V$ curves of the champion Control and Target devices to a two-diode equivalent circuit model[25] (Figure S9a,b). Following the analysis proposed by Guillemoles et al.[26] and Stolterfoht et al.,[27] the losses could be calculated and broken down into separate contributions (Figure 4d). First, the Shockley−Queisser limit was calculated from the band gap, which we determined from the inflection point of the IPCE spectrum (Figure S4). A band gap of 1.555 eV was obtained for both the Control and the Target devices, which was expected due to the small amount of MA^+ being incorporated,

https://doi.org/10.1021/acsenergylett.1c01754
ACS Energy Lett. 2021, 6, 3650−3660

thus having a limited effect on the band gap. The performance losses related to the radiative limit with respect to the Shockley–Queisser limit accounted for 0.21% (V_{OC} loss) + 9.3% (J_{SC} loss) = 9.51% for the control and 0.16% (V_{OC} loss) + 7.0% (J_{SC} loss) = 7.16% for the target device, The J_{SC} losses were mainly due to nonideal and parasitic absorption. Substantially lower nonradiative losses were observed upon the addition of MAI_3, decreasing from 17.9% (V_{OC} loss) + 8.1% (FF loss) = 26% in the control device to 11.1% (V_{OC} loss) + 7% (FF loss) = 18.1% in the target device. Transport losses manifested themselves in a further reduction of the FF. These transport-related FF losses of the Control and Target samples were 4.8 and 3.5%, respectively. These improvements in the FF are consistent with the enhanced charge carrier mobility in the Target.

To further confirm the role of nonradiative recombination, we measured absolute photoluminescence (PL) photon fluxes $\Phi_{PL}(E)$ of Control and Target films (Figure 4e). Following the established methods,[28] we calculated the photoluminescence quantum yields (PLQYs) as 1.53 and 0.61% for Target and Control samples, respectively. The enhancement in the PLQY for the Target films indicates the suppression of nonradiative recombination centers in the bulk of the perovskite. To gain further insights into the charge carrier dynamics, we performed time-resolved photoluminescence (TRPL) spectroscopy using laser excitation pulses of low fluences (<5 nJ/cm^2) so that bimolecular and Auger recombination were negligible.[29] The signal after t > 200 ns was dominated by a monoexponential decay (Figure 4f). Because it is impossible to distinguish between surface and bulk recombination, we modeled two extreme cases for the interpretation of the TRPL data in Figure 4f and Tables S3 and S4. In the first case, we assumed zero surface recombination, which means the decay is attributed solely to the bulk recombination with a fitted monomolecular recombination constant $k_1 = 2.0 \times 10^6$ s^{-1} (TRPL decay time or charge carrier lifetime: $\tau = 1/(2*k_1) = 250$ ns) for the Control and $k_1 = 1.0 \times 10^6$ s^{-1} ($\tau = 500$ ns) for the Target sample. Also, we estimated the lower limit of diffusion length (L_D) via $L_D = \sqrt{\frac{\mu k T \tau}{e}}$, where μ is the mobility and k, T, e, and τ are the Boltzmann constant, temperature, elementary charge, and charge carrier lifetime, respectively. The charge carrier mobility was calculated to be 39.5 cm^2 V^1 S^{-1} for the control and 45.5 cm^2 V^1 S^{-1} for the target at an excitation fluence of 16.91 μJ cm^{-2}. From these mobility values, we derived L_D = 0.72 μm for the control device and L_D = 1.07 μm for the target. In the second case, we assumed that the TRPL decays of both samples were dominated by surface recombination, with a surface recombination velocity S fitted as 120 cm/s for the control and 62 cm/s for the target sample. Both cases show that there is an enhancement in the charge carrier lifetime and suppression of nonradiative recombination in the Target sample. Overall, these results, acquired from TRTS, photovoltaic (PV) device loss analysis, n_{id}, PLQY, and TRPL measurements indicate that the addition of MAI_3 simultaneously reduces the nonradiative recombination rate and increases the charge carrier mobility, leading to the observed improvements in both the V_{OC} and FF.

Thermal and operational stability remains a major concern in PSCs.[30−32] Therefore, we carried out the stability test on the Control and Target by subjecting them to different stress conditions. First, we carried out a shelf-life test by keeping the devices in the dark under 10% RH. The Control and Target retained 74 and 93% of the initial performance after 800 h, respectively (Figure 5a). Second, we carried out a thermal stability test by keeping the devices at 50−55 °C under ambient conditions (25−35% RH). The Control and Target retained 28 and 60% of the initial performance after 300 h, respectively (Figure 5b). Lastly, we performed operational stability tests at MPP for 350 h under continuous 1 sun illumination. The Control and Target devices retained 57 and 89% of the initial performance, respectively. Typically, the defects are known to be responsible for the instability, and hence the improvement in the stability is likely the result of the improved optoelectronic properties and reduction in defects. This showed that our strategy with perovskite bulk engineering viaMAI_3 not only improves the performance of PSCs but also enhances the device stability under standard stress conditions. Furthermore, we performed the aging of the perovskite films at 50 °C at a relative humidity of ∼40−50% for 72 h and recorded the XRD and SEM of the fresh and aged films. We observed the formation of PbI_2 in control films, whereas the target film remained stable, as shown in Figure S10. In the top-view SEM (Figure S11) of the aged control film, we observed pin holes and secondary morphology with different contrasts, which could be PbI_2, whereas the morphology of the target samples was not significantly altered after aging. These results show that perovskite films with additive MAI_3 are much more stable than control films.

In summary, we employed MAI_3 as an additive in the perovskite precursor solution of metal halide perovskite absorber, affording the passivation of Pb^0 and charged defects, leading to the suppression of nonradiative recombination and an enhanced charge carrier mobility. As a result, we achieved a PCE exceeding 23% with the MAI_3-modulated Target, which also exhibited a remarkable improvement in stability with respect to the Control regardless of the external aging conditions (high temperature, ambient, MPP). The facile strategy provided in this work has the potential to stimulate other successful developments in the future

EXPERIMENTAL METHODS

Device Fabrication. Fluorine-doped tin oxide (FTO) glass substrates (TCO glass, NSG 10, Nippon sheet glass, Japan) were etched and cleaned by ultrasonication in Hellmanex (2%, deionized water), rinsed thoroughly with deionized water and ethanol, and then treated in oxygen plasma for 30 min. An approximately 30 to 25 nm blocking layer (TiO_2) was sprayed on the cleaned FTO at 450 °C using a commercial titanium diisopropoxide bis(acetylacetonate) solution (75% in 2-propanol, Sigma-Aldrich) diluted in anhydrous ethanol (1:10 volume ratio). A 150 nm mesoporous TiO_2 layer (diluted paste (1:6.5 wt ratio) (Dyesol 30NRD/ethanol)) was spin-coated at 5000 rpm for 15 s and then sintered at 450 °C for 30 min in dry air. The perovskite films were deposited using a single-step deposition method from the precursor solution, which was prepared in an argon atmosphere containing 1.45 M of FAI, MABr, PbI_2, and $PbBr_2$ in anhydrous dimethylformamide/dimethyl sulfoxide (4:1 (volume ratio)) to achieve the desired composition: $FA_{0.98}MA_{0.02}Pb(I_{0.98}Br_{0.02})_3$ (3% PbI_2 excess). For the additives, three stock solutions of 0.1 M were prepared of I_2, MAI, and MAI+I_2 by dissolving in IPA and stirred at 70 °C at different times. Then, each of them was added to the perovskite composition at different concentrations. The device fabrication was carried out inside a dry air box under controlled atmospheric conditions. Perovskite solution was

https://doi.org/10.1021/acsenergylett.1c01754
ACS Energy Lett. 2021, 6, 3650−3660

spin-coated in a two-step program at 1000 and 5000 rpm, respectively. 270 μL of chlorobenzene was dropped on the spinning substrate. This was followed by annealing of the films at 150 °C for 35 to 40 min. After the substrate was cooled, all films (control film included) were passivated by ethylammonium iodide (EAI) (3 mg mL^{-1}).[19] 90 mg of 2,2′,7,7′-tetrakis(*N*,*N*-di-*p*-methoxyphenylamine)-9,9-spirobifluorene (spiro-OMeTAD) was dissolved in 1 mL of chlorobenzene as a hole-transporting material (HTM) to complete the fabrication of the devices. The HTM was spin-coated at 5000 rpm for 30 s. The HTM was doped with bis(trifluoromethylsulfonyl)imide lithium salt (23.2 μL prepared by dissolving 520 mg of LiTFSI in 1 mL of acetonitrile) and 36 μL of 4-*tert*-butylpyridine. Finally, an ∼80 nm gold (Au) layer was thermally evaporated.

Device Characterization. The current−voltage (J−V) characteristics of the perovskite devices were recorded under ambient temperature and air conditions with a digital source meter (Keithley model 2400, USA). A 450 W xenon lamp (Oriel, USA) was used as the light source for photovoltaic (J−V) measurements. The spectral output of the lamp was filtered using a Schott K113 Tempax sunlight filter (Präzisions Glas & Optik, Germany) to reduce the mismatch between the simulated and the actual solar spectra to <2%. The light intensity ranged between 0.98 and 1sun. A photoactive area of 0.158 cm^2 was defined using a dark-colored metal mask.

Incident Photon-to-Current Efficiency. The IPCE was recorded under a constant white-light bias of ∼5 mW cm^{-2} supplied by an array of white light-emitting diodes (LEDs). The excitation beam coming from a 300 W xenon lamp (ILC Technology) was focused through a Gemini-180 double monochromator (Jobin Yvon) and chopped at ∼2 Hz. The signal was recorded using a model SR830 DSP lock-in amplifier (Stanford Research Systems).

Scanning Electron Microscopy. Scanning electron microscopy was performed on a ZEISS Merlin high-resolution (HR)-SEM.

X-ray Photoelectron Spectroscopy. XPS measurements were carried out on an Axis Supra apparatus (Kratos Analytical) using the monochromated Kα X-ray line of an aluminum anode. The pass energy was set to 20 eV with a step size of 0.1 eV. The samples were electrically grounded through the FTO substrate to limit the charging effects.

X-ray Powder Diffractions. X-ray patterns were recorded on a Bruker D8 Discover apparatus (Cu anode, λ = 1.54060 Å) in Bragg−Brentano geometry, equipped with a Johansson Kα_1 monochromator and a Lynxeye XE detector. Lattice parameters were extracted from profile fitting using TOPAS 5.

Time-Resolved Photoluminescence. The PL lifetime was measured via time-correlated single-photon counting (TCSPC) using a LifeSpec II (Edinburgh Instruments) fluorescence spectrometer with a picosecond pulsed diode laser (EPL-510, Edinburgh Instruments) at 510 nm wavelength, 85 ps pulse width, and 4.5 nJ/cm2 fluence.

Solid-State Nuclear Magnetic Resonance Measurements. ssNMR ^{1}H measurements were carried out at 900.14 MHz using a Bruker Avance Neo console and a 1.3 mm variable temperature cross-polarization magic-angle spinning (CPMAS) probe at a spin rate of 60 kHz. The measurements were taken using a standard echo sequence with an echo delay of one rotor period with 100 kHz radio frequency (RF) power. A delay time of five times T1 was used to obtain quantitative results. The spectra were baseline-corrected, and the areas were extracted using the multipeak fit tool in Origin Lab.

Long-Term Light Soaking Test. Stability measurements were performed with a Biologic MPG2 potentiostat under a full AM 1.5 sun equivalent white LED lamp. The devices were measured with an MPP tracking routine under continuous illumination at room temperature. The MPP was updated every 10 s by a standard perturb and observe method. Every minute, a J−V curve was recorded to track the evolution of individual J−V parameters.

Photoluminescence Quantum Yield. The PLQY was acquired following the procedure suggested by de Mello.[28] The samples were excited using a continuous-wave laser (OBIS LX, 660 nm) whose power was adjusted to match the photogeneration rate under 1 sun of illumination (0.324 mW, 0.786 mm effective beam full width at half-maximum (fwhm)). The signal was collected using an integrating sphere (Gigahertz Optik, UPB-150-ARTA) connected via a multimode, 400 μm diameter optical fiber (Thorlabs BFL44LS01) to a spectrometer (Andor, Kymera 193i). The system was spectrally calibrated using an irradiance calibration standard lamp (Gigahertz Optik, BN-LH250-V01).

Time-Resolved Terahertz Spectroscopy. TRTS measurements were conducted using a femtosecond visible pump−THz probe setup based on an amplified Ti:sapphire laser (Libra, Coherent) delivering 800 nm pulses with a pulse duration of 45 fs and a 1 kHz repetition rate. The fundamental output was split into three beams. The first was used to pump a white-light seeded optical parametric amplifier (OPerA Solo, Coherent), yielding the 580 nm pump beam. The second fundamental beam was used to generate the THz probe through a two-color plasma method.[33] The beam was focused using a fused silica lens (f = 75 mm) and passed through a 100 μm beta-barium borate (BBO) crystal to generate the second harmonic. The electric field of the two-color beam was strong enough, at the focal point, to form a plasma that radiated THz pulses (200 fs, 1−20 THz), which were subsequently collimated and focused onto the sample. The transmitted beam was subsequently detected using a homemade ABCD (air-based coherent detection) detector.[34] The final portion of the fundamental was used as the gate beam and was used to generate a second-harmonic signal proportional to that of the THz electric field measured with a photomultiplier tube (PMM01, Thorlabs). The second-harmonic generation (SHG) process took place inside an enclosed box with a butane atmosphere,[35] allowing for increased sensitivity when measuring the dynamics.

COMPUTATIONAL METHODS

Structural Relaxation. All computations related to structural relaxation were done at the DFT level of theory using Quantum ESPRESSO v6.6.[36−38] Apart from variable-cell relaxations, all relaxations applied the Perdew−Burke−Ernzerhof (PBE) functional using ultrasoft pseudopotentials from the pslibrary 1.0.0, a wave function cutoff of 60 Ry, a charge density cutoff of 480 Ry, a 6 × 6 × 1 k-point Monkhorst−Pack grid without offset, Gaussian spreading of 0.01 Ry, and the semiempirical Grimme's DFT-D3 van der Waals (vdW) correction. For the variable-cell relaxations, PBEsol was applied, and the remaining parameters were chosen to be the same as those above. The structural relaxation of the initial and final states for the addition reaction of MAI_3 onto $FAPbI_3$ was done in multiple steps. Initially, a 2 × 2 × 6 supercell of pure $FAPbI_3$ (without defects) was optimized using variable-cell relaxation. Next, 42 Å of empty space was

https://doi.org/10.1021/acsenergylett.1c01754
ACS Energy Lett. 2021, 6, 3650−3660

introduced along the z direction to generate a realistic surface model Pb−I as a terminating layer. Furthermore, two iodides next to a common Pb located at the surface were removed, two electrons were added, and the structure was reoptimized. Upon relaxation of an isolated MAI_3, this molecule was added in various orientations at distances of 3.0 to 3.5 Å with respect to the halide vacancies. After undergoing another relaxation, this gave a set of seven final states, each with the two initial defects filled by iodides and the third iodide attached to one of the Pb ions on the surface (SI). The initial reference state was constructed in a similar manner by placing the optimized MAI_3 at a distance of 9−12 Å from the surface with three different orientations, each of which underwent a relaxation. For both the initial and final states, the lowest energy structure was used for the charge analysis.

Bader Charge Analysis. A Gaussian CUBE file was generated based on the optimized density using the *PostProc* package from Quantum ESPRESSO. From the Gaussian CUBE file, the Bader charges were computed using the program developed by Henkelman's group.[39]

Simulations of Phase Transition. Classical MD simulations were performed in an isothermal−isobaric ensemble similar to our previous studies.[40,41] All simulations were performed with the Large-scale Atomic/Molecular Massively Parallel Simulator (LAMMPS) code (2017-03-31).[40] We used a 1.0 nm cutoff for nonbonded interactions, SHAKE[41] for constraints, and particle−particle−particle−mesh Ewald for electrostatic interactions. We used a velocity rescaling thermostat[42] with a relaxation time of 0.1 ps and a Parrinello−Rahman barostat[43] to keep the pressure at atmospheric pressure with a relaxation time of 10 ps.

■ ASSOCIATED CONTENT

Supporting Information

The Supporting Information is available free of charge at https://pubs.acs.org/doi/10.1021/acsenergylett.1c01754.

Additional J−V data, SEM images, XPS, XRD, NMR, TRTS, and computational data, simulated J−V analysis of loss mechanism, and stability data for perovskite films (PDF)

■ AUTHOR INFORMATION

Corresponding Author

Michael Grätzel − *Laboratory of Photonics and Interfaces, Institute of Chemical Sciences and Engineering, School of Basic Sciences, Ecole Polytechnique Fédérale de Lausanne, CH-1015 Lausanne, Switzerland;* orcid.org/0000-0002-0068-0195; Email: michael.graetzel@epfl.ch

Authors

Essa A. Alharbi − *Laboratory of Photonics and Interfaces, Institute of Chemical Sciences and Engineering, School of Basic Sciences, Ecole Polytechnique Fédérale de Lausanne, CH-1015 Lausanne, Switzerland;* orcid.org/0000-0003-1533-5906

Anurag Krishna − *Laboratory of Photomolecular Science, Institute of Chemical Science and Engineering, School of Basic Sciences, Ecole Polytechnique Fédérale de Lausanne, CH-1015 Lausanne, Switzerland;* orcid.org/0000-0001-7255-7412

Thomas P. Baumeler − *Laboratory of Photonics and Interfaces, Institute of Chemical Sciences and Engineering, School of Basic Sciences, Ecole Polytechnique Fédérale de Lausanne, CH-1015 Lausanne, Switzerland*

Mathias Dankl − *Laboratory of Computational Chemistry and Biochemistry, Institute of Chemical Sciences and Engineering, École Polytechnique Fédérale de Lausanne (EPFL), CH-1015 Lausanne, Switzerland*

George C. Fish − *Photochemical Dynamics Group, Institute of Chemical Sciences and Engineering, and Lausanne Centre for Ultrafast Science, École Polytechnique Fédérale de Lausanne, CH-1015 Lausanne, Switzerland*

Felix Eickemeyer − *Laboratory of Photonics and Interfaces, Institute of Chemical Sciences and Engineering, School of Basic Sciences, Ecole Polytechnique Fédérale de Lausanne, CH-1015 Lausanne, Switzerland;* orcid.org/0000-0003-0855-9944

Olivier Ouellette − *Laboratory of Photonics and Interfaces, Institute of Chemical Sciences and Engineering, School of Basic Sciences, Ecole Polytechnique Fédérale de Lausanne, CH-1015 Lausanne, Switzerland*

Paramvir Ahlawat − *Laboratory of Computational Chemistry and Biochemistry, Institute of Chemical Sciences and Engineering, École Polytechnique Fédérale de Lausanne (EPFL), CH-1015 Lausanne, Switzerland;* orcid.org/0000-0003-2355-3663

Viktor Škorjanc − *Laboratory of Photonics and Interfaces, Institute of Chemical Sciences and Engineering, School of Basic Sciences, Ecole Polytechnique Fédérale de Lausanne, CH-1015 Lausanne, Switzerland*

Elsa John − *Laboratory of Photomolecular Science, Institute of Chemical Science and Engineering, School of Basic Sciences, Ecole Polytechnique Fédérale de Lausanne, CH-1015 Lausanne, Switzerland*

Bowen Yang − *Laboratory of Photomolecular Science, Institute of Chemical Science and Engineering, School of Basic Sciences, Ecole Polytechnique Fédérale de Lausanne, CH-1015 Lausanne, Switzerland;* orcid.org/0000-0002-9471-3452

Lukas Pfeifer − *Laboratory of Photonics and Interfaces, Institute of Chemical Sciences and Engineering, School of Basic Sciences, Ecole Polytechnique Fédérale de Lausanne, CH-1015 Lausanne, Switzerland;* orcid.org/0000-0002-8461-3909

Claudia Esther Avalos − *Laboratory of Magnetic Resonance, Institute of Chemical Sciences and Engineering, School of Basic Sciences, Ecole Polytechnique Fédérale de Lausanne, CH-1015 Lausanne, Switzerland*

Linfeng Pan − *Laboratory of Photomolecular Science, Institute of Chemical Science and Engineering, School of Basic Sciences, Ecole Polytechnique Fédérale de Lausanne, CH-1015 Lausanne, Switzerland*

Mounir Mensi − *Institute of Chemical Sciences and Engineering (ISIC), École Polytechnique Fédérale de Lausanne, CH-1950 Sion, Switzerland*

Pascal Alexander Schouwink − *Institute of Chemical Sciences and Engineering (ISIC), École Polytechnique Fédérale de Lausanne, CH-1950 Sion, Switzerland*

Jacques-E. Moser − *Photochemical Dynamics Group, Institute of Chemical Sciences and Engineering, and Lausanne Centre for Ultrafast Science, École Polytechnique Fédérale de Lausanne, CH-1015 Lausanne, Switzerland*

Anders Hagfeldt − *Laboratory of Photomolecular Science, Institute of Chemical Science and Engineering, School of Basic Sciences, Ecole Polytechnique Fédérale de Lausanne, CH-*

https://doi.org/10.1021/acsenergylett.1c01754
ACS Energy Lett. 2021, 6, 3650−3660

1015 Lausanne, Switzerland; orcid.org/0000-0001-6725-8856

Ursula Rothlisberger − *Laboratory of Computational Chemistry and Biochemistry, Institute of Chemical Sciences and Engineering, École Polytechnique Fédérale de Lausanne (EPFL), CH-1015 Lausanne, Switzerland;* orcid.org/0000-0002-1704-8591

Shaik M. Zakeeruddin − *Laboratory of Photonics and Interfaces, Institute of Chemical Sciences and Engineering, School of Basic Sciences, Ecole Polytechnique Fédérale de Lausanne, CH-1015 Lausanne, Switzerland*

Complete contact information is available at: https://pubs.acs.org/10.1021/acsenergylett.1c01754

Author Contributions

E.A.A. and M.G. conceived the idea of the work. E.A.A. designed the project and fabricated and optimized the solar cell devices. E.A.A. and A.K. planned the experiments and characterization, analyzed the data, and wrote the manuscript. T.P.B., V.S., and A.K. contributed to the device fabrication. A.K. recorded the stability measurements. M.D., P.A., and U.R. were responsible for the DFT calculations, charge analysis, energy computations, and molecular dynamics simulations. L.P. and E.J. helped with the chemical analysis of the additives. B.Y. recorded the SEM, and P.A.S. performed the XRD measurements. M.M. and L.P. recorded the XPS measurements. C.E.A. carried out the ssNMR measurement and analysis. O.O. recorded the PLQY and TRPL measurements and analyzed the PLQY data. F.E. analyzed the TRPL data. G.C.F. and J.E.M. performed and analyzed the TRTS measurements. M.G. and S.M.Z. supervised the project and discussed the results. All authors contributed to the preparation of the manuscript.

Notes

The authors declare no competing financial interest.

■ ACKNOWLEDGMENTS

E.A.A. gratefully acknowledges King Abdulaziz City for Science and Technology (KACST) for a fellowship. A.K. acknowledges funding from the European Union's Horizon 2020 Research and Innovation program under the Marie Skłodowska-Curie grant agreement no. 843453. T.P.B. acknowledges support from the Swiss National Science Foundation (project no. IZJSZ2_180176). U.R. acknowledges Swiss National Science Foundation grant no. 200020-185092 and the NCCR-MUST for funding and computational resources from the Swiss National Computing Centre CSCS. G.C.F. and J.-E.M. are grateful to the SNF (grant no. 200021_175729) and NCCR-MUST for support. O.O. acknowledges funding from the National Sciences and Engineering Research Council of Canada. B.Y. acknowledges funding from the European Union's Horizon 2020 research and innovation programme under grant agreement no. 764047.

■ REFERENCES

(1) Kojima, A.; Teshima, K.; Shirai, Y.; Miyasaka, T. Organometal Halide Perovskites as Visible-Light Sensitizers for Photovoltaic Cells. *J. Am. Chem. Soc.* **2009**, *131* (17), 6050−6051.

(2) Yoo, J. J.; Seo, G.; Chua, M. R.; Park, T. G.; Lu, Y.; Rotermund, F.; Kim, Y. K.; Moon, C. S.; Jeon, N. J.; Correa-Baena, J. P.; Bulović, V.; Shin, S. S.; Bawendi, M. G.; Seo, J. Efficient Perovskite Solar Cells via Improved Carrier Management. *Nature* **2021**, *590* (7847), 587−593.

(3) Hui, W.; Chao, L.; Lu, H.; Xia, F.; Wei, Q.; Su, Z.; Niu, T.; Tao, L.; Du, B.; Li, D.; Wang, Y.; Dong, H.; Zuo, S.; Li, B.; Shi, W.; Ran, X.; Li, P.; Zhang, H.; Wu, Z.; Ran, C.; Song, L.; Xing, G.; Gao, X.; Zhang, J.; Xia, Y.; Chen, Y.; Huang, W. Stabilizing Black-Phase Formamidinium Perovskite Formation at Room Temperature and High Humidity. *Science* **2021**, *371* (6536), 1359−1364.

(4) *Best Research-Cell Efficiency Chart | Photovoltaic Research | NREL.* https://www.nrel.gov/pv/cell-efficiency.html (accessed 2021)

(5) Zhao, Y.; Zhu, P.; Huang, S.; Tan, S.; Wang, M.; Wang, R.; Xue, J.; Han, T. H.; Lee, S. J.; Zhang, A.; Huang, T.; Cheng, P.; Meng, D.; Lee, J. W.; Marian, J.; Zhu, J.; Yang, Y. Molecular Interaction Regulates the Performance and Longevity of Defect Passivation for Metal Halide Perovskite Solar Cells. *J. Am. Chem. Soc.* **2020**, *142* (47), 20071−20079.

(6) Xue, J.; Wang, R.; Yang, Y. The Surface of Halide Perovskites from Nano to Bulk. *Nature Reviews Materials* **2020**, *5*, 809−827.

(7) Liu, N.; Yam, C. Y. First-Principles Study of Intrinsic Defects in Formamidinium Lead Triiodide Perovskite Solar Cell Absorbers. *Phys. Chem. Chem. Phys.* **2018**, *20* (10), 6800−6804.

(8) Wang, L.; Zhou, H.; Hu, J.; Huang, B.; Sun, M.; Dong, B.; Zheng, G.; Huang, Y.; Chen, Y.; Li, L.; Xu, Z.; Li, N.; Liu, Z.; Chen, Q.; Sun, L. D.; Yan, C. H. A Eu3+ - Eu2+ Ion Redox Shuttle Imparts Operational Durability to Pb-I Perovskite Solar Cells. *Science* **2019**, *363* (6424), 265−270.

(9) Kim, G. Y.; Senocrate, A.; Yang, T. Y.; Gregori, G.; Grätzel, M.; Maier, J. Large Tunable Photoeffect on Ion Conduction in Halide Perovskites and Implications for Photodecomposition. *Nat. Mater.* **2018**, *17* (5), 445−449.

(10) Alharbi, E. A.; Baumeler, T. P.; Krishna, A.; Alyamani, A. Y.; Eickemeyer, F. T.; Ouellette, O.; Pan, L.; Alghamdi, F. S.; Wang, Z.; Alotaibi, M. H.; Yang, B.; Almalki, M.; Mensi, M. D.; Albrithen, H.; Albadri, A.; Hagfeldt, A.; Zakeeruddin, S. M.; Grätzel, M. Formation of High-Performance Multi-Cation Halide Perovskites Photovoltaics by δ-CsPbI3/δ-RbPbI3 Seed-Assisted Heterogeneous Nucleation. *Adv. Energy Mater.* **2021**, *11*, 2003785.

(11) Alharbi, E. A.; Dar, M. I.; Arora, N.; Alotaibi, M. H.; Alzhrani, Y. A.; Yadav, P.; Tress, W.; Alyamani, A.; Albadri, A.; Zakeeruddin, S. M.; Grätzel, M. Perovskite Solar Cells Yielding Reproducible Photovoltage of 1.20 V. *Research* **2019**, *2019*, 1−9.

(12) Yadav, P.; Dar, M. I.; Arora, N.; Alharbi, E. A.; Giordano, F.; Zakeeruddin, S. M.; Grätzel, M. The Role of Rubidium in Multiple-Cation-Based High-Efficiency Perovskite Solar Cells. *Adv. Mater.* **2017**, *29* (40), 1701077.

(13) Baumeler, T.; Arora, N.; Hinderhofer, A.; Akin, S.; Greco, A.; Abdi-Jalebi, M.; Shivanna, R.; Uchida, R.; Liu, Y.; Schreiber, F.; Zakeeruddin, S. M.; Friend, R. H.; Graetzel, M.; Dar, M. I. Minimizing the Trade-Off between Photocurrent and Photovoltage in Triple-Cation Mixed-Halide Perovskite Solar Cells. *J. Phys. Chem. Lett.* **2020**, *11* (23), 10188−10195.

(14) Zhu, H.; Liu, Y.; Eickemeyer, F. T.; Pan, L.; Ren, D.; Ruiz-Preciado, M. A.; Carlsen, B.; Yang, B.; Dong, X.; Wang, Z.; Liu, H.; Wang, S.; Zakeeruddin, S. M.; Hagfeldt, A.; Dar, M. I.; Li, X.; Grätzel, M. Tailored Amphiphilic Molecular Mitigators for Stable Perovskite Solar Cells with 23.5% Efficiency. *Adv. Mater.* **2020**, *32* (12), 1907757.

(15) Liu, Y.; Akin, S.; Pan, L.; Uchida, R.; Arora, N.; Milic, J. V.; Hinderhofer, A.; Schreiber, F.; Uhl, A. R.; Zakeeruddin, S. M.; Hagfeldt, A.; Dar, M. I.; Gratzel, M. Ultrahydrophobic 3D/2D Fluoroarene Bilayer-Based Water-Resistant Perovskite Solar Cells with Efficiencies Exceeding 22%. *Sci. Adv.* **2019**, *5* (6), No. eaaw2543.

(16) Tan, F.; Tan, H.; Saidaminov, M. I.; Wei, M.; Liu, M.; Mei, A.; Li, P.; Zhang, B.; Tan, C. S.; Gong, X.; Zhao, Y.; Kirmani, A. R.; Huang, Z.; Fan, J. Z.; Quintero-Bermudez, R.; Kim, J.; Zhao, Y.; Voznyy, O.; Gao, Y.; Zhang, F.; Richter, L. J.; Lu, Z. H.; Zhang, W.; Sargent, E. H. In Situ Back-Contact Passivation Improves Photovoltage and Fill Factor in Perovskite Solar Cells. *Adv. Mater.* **2019**, *31* (14), 1807435.

(17) Hou, Y.; Aydin, E.; De Bastiani, M.; Xiao, C.; Isikgor, F. H.; Xue, D. J.; Chen, B.; Chen, H.; Bahrami, B.; Chowdhury, A. H.;

Johnston, A.; Baek, S. W.; Huang, Z.; Wei, M.; Dong, Y.; Troughton, J.; Jalmood, R.; Mirabelli, A. J.; Allen, T. G.; Van Kerschaver, E.; Saidaminov, M. I.; Baran, D.; Qiao, Q.; Zhu, K.; De Wolf, S.; Sargent, E. H. Efficient Tandem Solar Cells with Solution-Processed Perovskite on Textured Crystalline Silicon. *Science* **2020**, *367* (6482), 1135−1140.

(18) Li, Y.; Wu, H.; Qi, W.; Zhou, X.; Li, J.; Cheng, J.; Zhao, Y.; Li, Y.; Zhang, X. Passivation of Defects in Perovskite Solar Cell: From a Chemistry Point of View. *Nano Energy* **2020**, *77*, 105237.

(19) Alharbi, E. A.; Alyamani, A. Y.; Kubicki, D. J.; Uhl, A. R.; Walder, B. J.; Alanazi, A. Q.; Luo, J.; Burgos-Caminal, A.; Albadri, A.; Albrithen, H.; Alotaibi, M. H.; Moser, J.-E.; Zakeeruddin, S. M.; Giordano, F.; Emsley, L.; Grätzel, M. Atomic-Level Passivation Mechanism of Ammonium Salts Enabling Highly Efficient Perovskite Solar Cells. *Nat. Commun.* **2019**, *10* (1), 3008.

(20) Lin, Y. H.; Sakai, N.; Da, P.; Wu, J.; Sansom, H. C.; Ramadan, A. J.; Mahesh, S.; Liu, J.; Oliver, R. D. J.; Lim, J.; Aspitarte, L.; Sharma, K.; Madhu, P. K.; Morales-Vilches, A. B.; Nayak, P. K.; Bai, S.; Gao, F.; Grovenor, C. R. M.; Johnston, M. B.; Labram, J. G.; Durrant, J. R.; Ball, J. M.; Wenger, B.; Stannowski, B.; Snaith, H. J. A Piperidinium Salt Stabilizes Efficient Metal-Halide Perovskite Solar Cells. *Science (Washington, DC, U. S.)* **2020**, *369* (6499), 96−102.

(21) Turkevych, I.; Kazaoui, S.; Belich, N. A.; Grishko, A. Y.; Fateev, S. A.; Petrov, A. A.; Urano, T.; Aramaki, S.; Kosar, S.; Kondo, M.; Goodilin, E. A.; Graetzel, M.; Tarasov, A. B. Strategic Advantages of Reactive Polyiodide Melts for Scalable Perovskite Photovoltaics. *Nat. Nanotechnol.* **2019**, *14* (1), 57−63.

(22) Afrooz, M.; Dehghani, H. Effects of Triphenyl Phosphate as an Inexpensive Additive on the Photovoltaic Performance of Dye-Sensitized Nanocrystalline TiO2 Solar Cells. *RSC Adv.* **2015**, *5* (62), 50483−50493.

(23) Ahlawat, P.; Dar, M. I.; Piaggi, P.; Grätzel, M.; Parrinello, M.; Rothlisberger, U. Atomistic Mechanism of the Nucleation of Methylammonium Lead Iodide Perovskite from Solution. *Chem. Mater.* **2020**, *32* (1), 529−536.

(24) Ahlawat, P.; Hinderhofer, A.; Alharbi, E. A.; Lu, H.; Ummadisingu, A.; Niu, H.; Invernizzi, M.; Zakeeruddin, S. M.; Dar, M. I.; Schreiber, F.; Hagfeldt, A.; Grätzel, M.; Rothlisberger, U.; Parrinello, M. A Combined Molecular Dynamics and Experimental Study of Two-Step Process Enabling Low-Temperature Formation of Phase-Pure α-FAPbI 3. *Sci. Adv.* **2021**, *7* (17), No. eabe3326.

(25) Zhang, C.; Zhang, J.; Hao, Y.; Lin, Z.; Zhu, C. A Simple and Efficient Solar Cell Parameter Extraction Method from a Single Current-Voltage Curve. *J. Appl. Phys.* **2011**, *110* (6), No. 064504.

(26) Guillemoles, J. F.; Kirchartz, T.; Cahen, D.; Rau, U. Guide for the Perplexed to the Shockley−Queisser Model for Solar Cells. *Nat. Photonics* **2019**, *13*, 501−505.

(27) Stolterfoht, M.; Grischek, M.; Caprioglio, P.; Wolff, C. M.; Gutierrez-Partida, E.; Peña-Camargo, F.; Rothhardt, D.; Zhang, S.; Raoufi, M.; Wolansky, J.; Abdi-Jalebi, M.; Stranks, S. D.; Albrecht, S.; Kirchartz, T.; Neher, D. How To Quantify the Efficiency Potential of Neat Perovskite Films: Perovskite Semiconductors with an Implied Efficiency Exceeding 28%. *Adv. Mater.* **2020**, *32* (17), 2000080.

(28) de Mello, J. C.; Wittmann, H. F.; Friend, R. H. An Improved Experimental Determination of External Photoluminescence Quantum Efficiency. *Adv. Mater.* **1997**, *9* (3), 230−232.

(29) Kirchartz, T.; Márquez, J. A.; Stolterfoht, M.; Unold, T. Photoluminescence-Based Characterization of Halide Perovskites for Photovoltaics. *Adv. Energy Mater.* **2020**, *10* (26), 1904134.

(30) Tress, W.; Domanski, K.; Carlsen, B.; Agarwalla, A.; Alharbi, E. A.; Graetzel, M.; Hagfeldt, A. Performance of Perovskite Solar Cells under Simulated Temperature-Illumination Real-World Operating Conditions. *Nat. Energy* **2019**, *4* (7), 568−574.

(31) Yadav, P.; Prochowicz, D.; Alharbi, E. A.; Zakeeruddin, S. M.; Grätzel, M. Intrinsic and Interfacial Kinetics of Perovskite Solar Cells under Photo and Bias-Induced Degradation and Recovery. *J. Mater. Chem. C* **2017**, *5* (31), 7799−7805.

(32) Domanski, K.; Alharbi, E. A.; Hagfeldt, A.; Grätzel, M.; Tress, W. Systematic Investigation of the Impact of Operation Conditions on the Degradation Behaviour of Perovskite Solar Cells. *Nat. Energy* **2018**, *3* (1), 61−67.

(33) Kim, K. Y.; Taylor, A. J.; Glownia, J. H.; Rodriguez, G. Coherent Control of Terahertz Supercontinuum Generation in Ultrafast Laser-Gas Interactions. *Nat. Photonics* **2008**, *2* (10), 605−609.

(34) Karpowicz, N.; Dai, J.; Lu, X.; Chen, Y.; Yamaguchi, M.; Zhao, H.; Zhang, X. C.; Zhang, L.; Zhang, C.; Price-Gallagher, M.; Fletcher, C.; Mamer, O.; Lesimple, A.; Johnson, K. Coherent Heterodyne Time-Domain Spectrometry Covering the Entire "Terahertz Gap. *Appl. Phys. Lett.* **2008**, *92* (1), No. 011131.

(35) Lu, X.; Zhang, X. C. Terahertz Wave Gas Photonics: Sensing with Gases. *J. Infrared, Millimeter, Terahertz Waves* **2011**, *32* (5), 562−569.

(36) Giannozzi, P.; Baroni, S.; Bonini, N.; Calandra, M.; Car, R.; Cavazzoni, C.; Ceresoli, D.; Chiarotti, G. L.; Cococcioni, M.; Dabo, I.; Dal Corso, A.; De Gironcoli, S.; Fabris, S.; Fratesi, G.; Gebauer, R.; Gerstmann, U.; Gougoussis, C.; Kokalj, A.; Lazzeri, M.; Martin-Samos, L.; Marzari, N.; Mauri, F.; Mazzarello, R.; Paolini, S.; Pasquarello, A.; Paulatto, L.; Sbraccia, C.; Scandolo, S.; Sclauzero, G.; Seitsonen, A. P.; Smogunov, A.; Umari, P.; Wentzcovitch, R. M. QUANTUM ESPRESSO: A Modular and Open-Source Software Project for Quantum Simulations of Materials. *J. Phys.: Condens. Matter* **2009**, *21* (39), 395502.

(37) Giannozzi, P.; Andreussi, O.; Brumme, T.; Bunau, O.; Buongiorno Nardelli, M.; Calandra, M.; Car, R.; Cavazzoni, C.; Ceresoli, D.; Cococcioni, M.; Colonna, N.; Carnimeo, I.; Dal Corso, A.; De Gironcoli, S.; Delugas, P.; Distasio, R. A.; Ferretti, A.; Floris, A.; Fratesi, G.; Fugallo, G.; Gebauer, R.; Gerstmann, U.; Giustino, F.; Gorni, T.; Jia, J.; Kawamura, M.; Ko, H. Y.; Kokalj, A.; Kücükbenli, E.; Lazzeri, M.; Marsili, M.; Marzari, N.; Mauri, F.; Nguyen, N. L.; Nguyen, H. V.; Otero-De-La-Roza, A.; Paulatto, L.; Poncé, S.; Rocca, D.; Sabatini, R.; Santra, B.; Schlipf, M.; Seitsonen, A. P.; Smogunov, A.; Timrov, I.; Thonhauser, T.; Umari, P.; Vast, N.; Wu, X.; Baroni, S. Advanced Capabilities for Materials Modelling with Quantum ESPRESSO. *J. Phys.: Condens. Matter* **2017**, *29* (46), 465901.

(38) Giannozzi, P.; Baseggio, O.; Bonfà, P.; Brunato, D.; Car, R.; Carnimeo, I.; Cavazzoni, C.; De Gironcoli, S.; Delugas, P.; Ferrari Ruffino, F.; Ferretti, A.; Marzari, N.; Timrov, I.; Urru, A.; Baroni, S. Quantum ESPRESSO toward the Exascale. *J. Chem. Phys.* **2020**, *152* (15), 154105.

(39) Henkelman, G.; Arnaldsson, A.; Jónsson, H. A Fast and Robust Algorithm for Bader Decomposition of Charge Density. *Comput. Mater. Sci.* **2006**, *36* (3), 354−360.

(40) Plimpton, S. Fast Parallel Algorithms for Short-Range Molecular Dynamics. *J. Comput. Phys.* **1995**, *117* (1), 1−19.

(41) Ryckaert, J. P.; Ciccotti, G.; Berendsen, H. J. C. Numerical Integration of the Cartesian Equations of Motion of a System with Constraints: Molecular Dynamics of n-Alkanes. *J. Comput. Phys.* **1977**, *23* (3), 327−341.

(42) Bussi, G.; Donadio, D.; Parrinello, M. Canonical Sampling through Velocity Rescaling. *J. Chem. Phys.* **2007**, *126* (1), 014101.

(43) Parrinello, M.; Rahman, A. Polymorphic Transitions in Single Crystals: A New Molecular Dynamics Method. *J. Appl. Phys.* **1981**, *52* (12), 7182−7190.

https://doi.org/10.1021/acsenergylett.1c01754
ACS Energy Lett. 2021, 6, 3650−3660

Supporting information

Methylammonium triiodide for defect engineering of high-efficiency perovskite solar cells

Essa A. Alharbi[1], Anurag Krishna[2], Thomas P. Baumeler[1], Mathias Dankl[3], George C. Fish[4], Felix Eickemeyer[1], Olivier Ouellette[1], Paramvir Ahlawat[3], Viktor Škorjanc[1], Elsa John[2], Bowen Yang[2], Lukas Pfeifer[1], Claudia Esther Avalos[5], Linfeng Pan[2], Mounir Mensi[6], Pascal Alexander Schouwink[6], Jacques-E Moser[4], Anders Hagfeldt[2], Ursula Rothlisberger[3], Shaik M. Zakeeruddin[1] and Michael Grätzel[1*]

[1] Laboratory of Photonics and Interfaces, Institute of Chemical Sciences and Engineering, School of Basic Sciences, Ecole Polytechnique Fédérale de Lausanne, CH-1015, Lausanne, Switzerland

[2] Laboratory of Photomolecular Science, Institute of Chemical Science and Engineering, School of Basic Sciences, Ecole Polytechnique Fédérale de Lausanne, CH-1015, Lausanne, Switzerland

[3] Laboratory of Computational Chemistry and Biochemistry, Institute of Chemical Sciences and Engineering, École Polytechnique Fédérale de Lausanne (EPFL), Lausanne, Switzerland

[4] Photochemical Dynamics Group, Institute of Chemical Sciences and Engineering, and Lausanne Centre for Ultrafast Science, École Polytechnique Fédérale de Lausanne, CH-1015, Lausanne, Switzerland

[5]Laboratory of Magnetic Resonance, Institute of Chemical Sciences and Engineering, School of Basic Sciences, Ecole Polytechnique Fédérale de Lausanne, CH-1015, Lausanne, Switzerland

[6] Institute of Chemical Sciences and Engineering (ISIC), École Polytechnique Fédérale de Lausanne, CH-1950 Sion, Switzerland

[*] Correspondence to Michael Grätzel (michael.graetzel@epfl.ch)

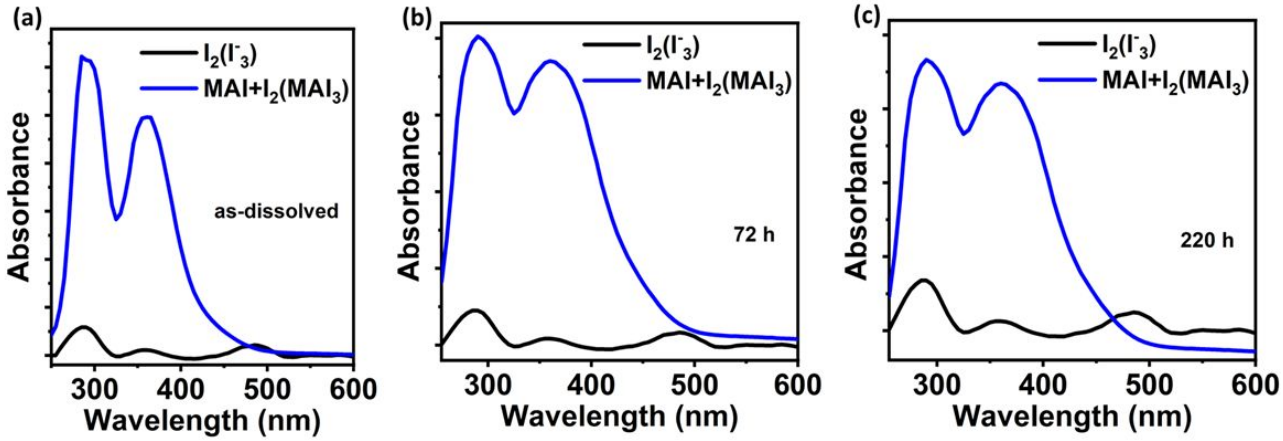

Figure S1. (a), (b), and (c) UV-Vis absorbance of I_2, MAI, and MAI+I_2 at a different time interval.

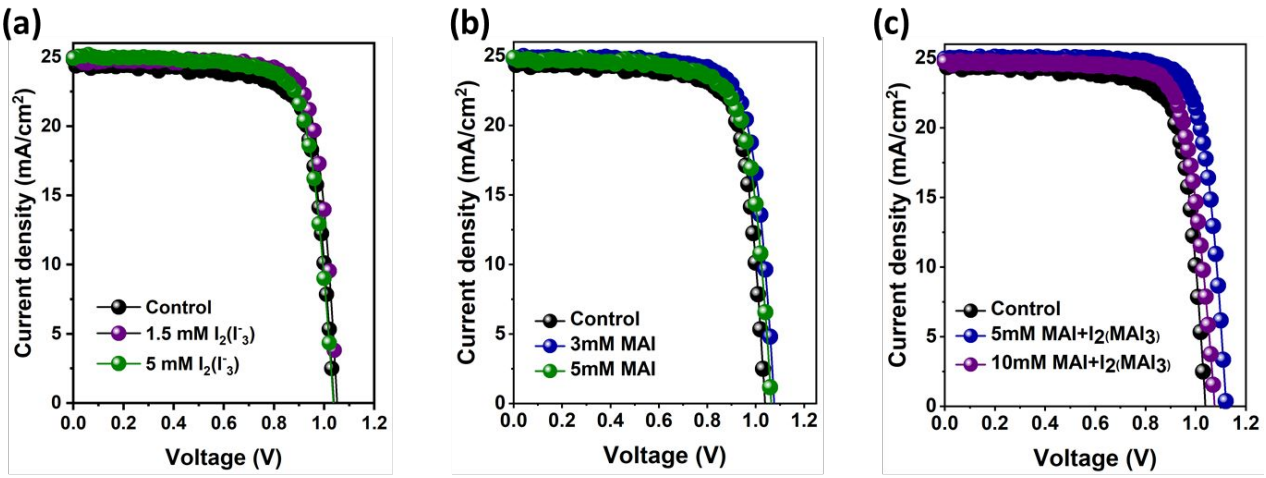

(d)

V_{oc} (V)	J_{sc} (mA/cm^2)	FF(%)	PCE(%)	V_{oc} (V)	J_{sc} (mA/cm^2)	FF(%)	PCE(%)
Control				3mM MAI			
1.045	25.06	76.7	20.32	1.08	25.03	77.2	21.08
1.5 mM (I_2) I^-_3				5mM MAI			
1.052	25.20	79.5	21.43	1.064	25.08	75.0	20.02
5mM (I_2) I^-_3				5mM (MAI+I_2) MAI_3			
1.037	25.16	76.6	20.24	1.13	25.20	81.4	23.46
				10mM (MAI+I_2) MAI_3			
				1.07	24.97	77.0	20.61

Figure S2. (a), (b), and (c) J-V curve of the optimized devices for each additive and (d) summarized J-V results for each additive.

(a)

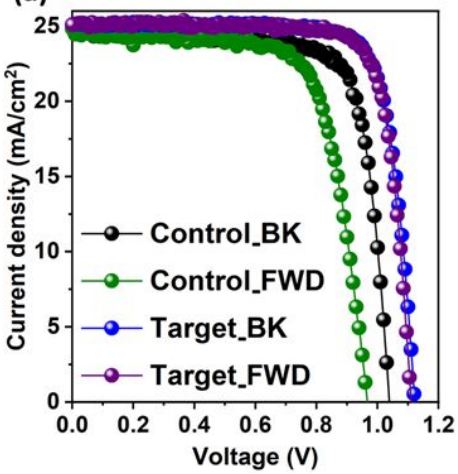

(b)

	V_{oc} (V)	J_{sc} (mA/cm²)	FF(%)	PCE(%)
Control				
BK	1.032	24.96	76.0	19.77
FWD	0.967	24.92	71.0	17.28
Target				
BK	1.124	25.10	80.9	23.10
FWD	1.116	25.08	80.2	22.67

Figure S3. J-V curves and (b) Summarized result J-V of the Control and target at backward and forward scan.

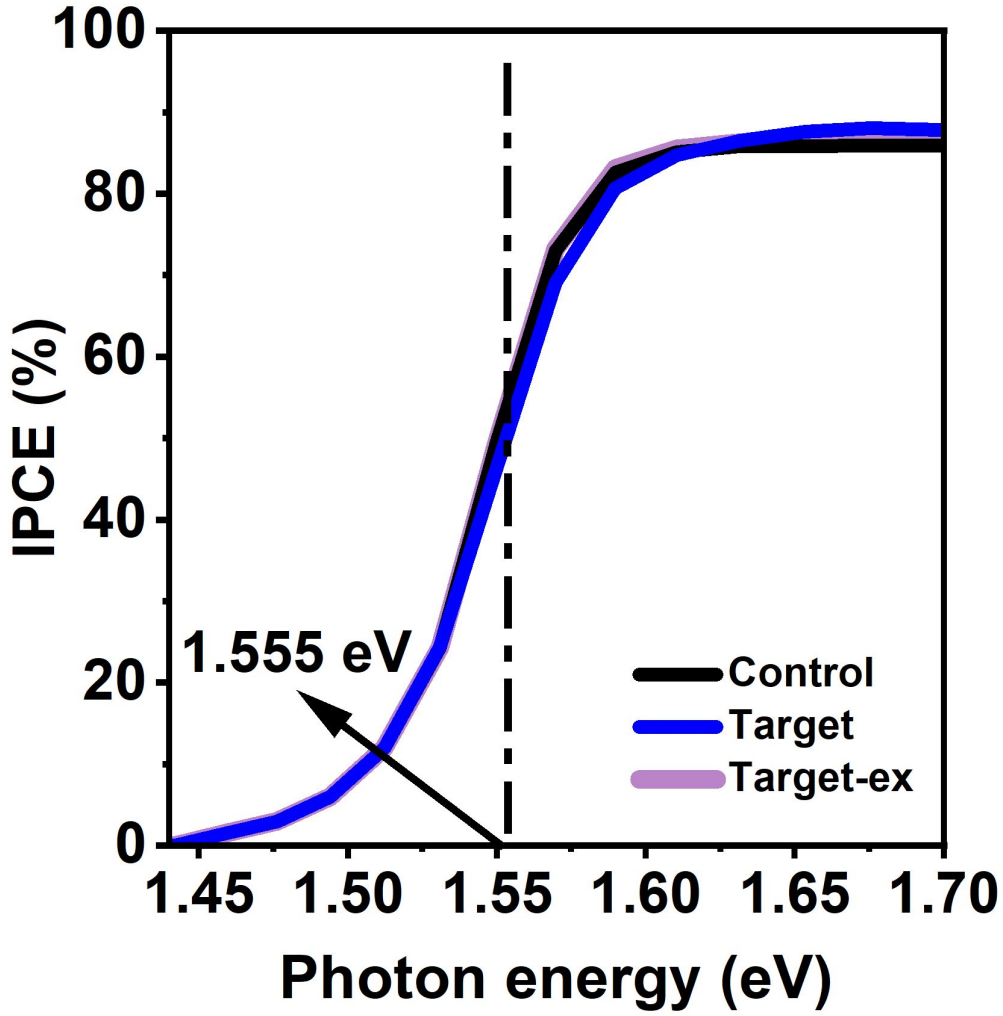

Figure S4. Bandgap extracted from IPCE of solar cells by taking the inflection point.

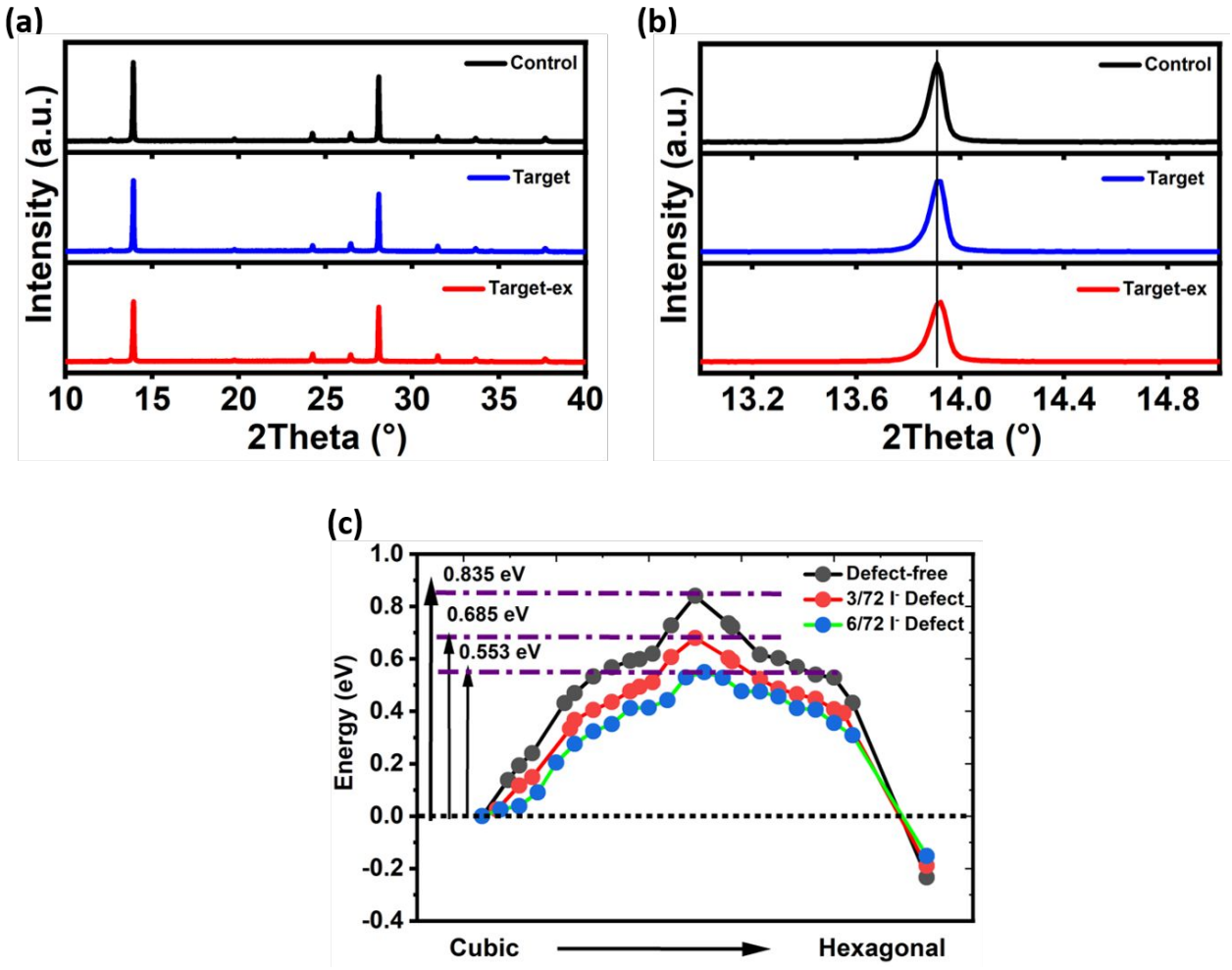

Figure S5. (a) and (b) XRD of Control, Target, and Target-ex; (c) Effect of V_I defects on the computed energy pathway for the phase transition from the cubic-to-hexagonal phase. These simulations are performed with classical force fields modified from earlier reported studies[1].

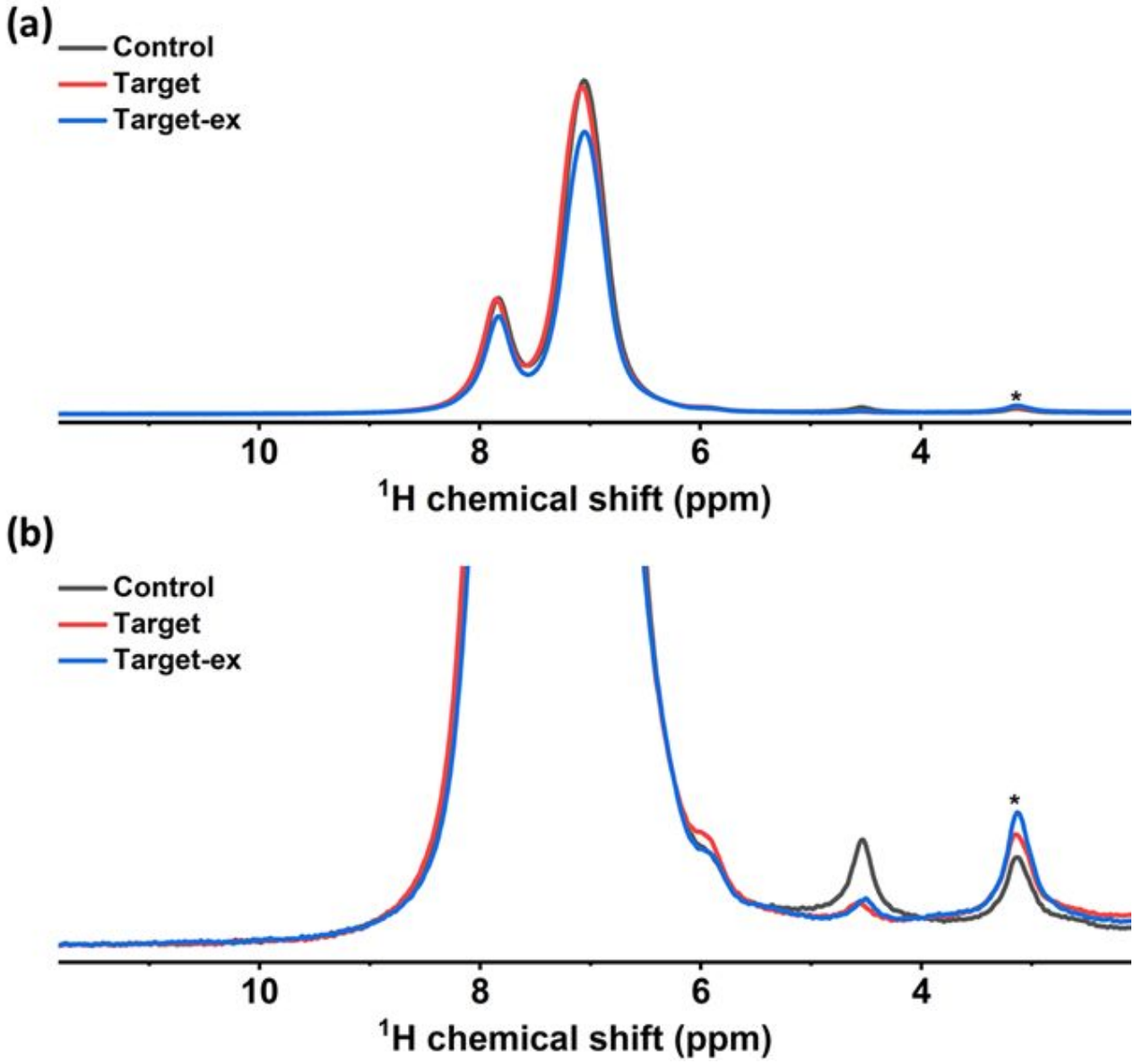

Figure S6. (a) and (b) Solid-state ^{1}H MAS NMR measurements at 21.1 T, 300 K, and 60 kHz MAS of Control, Target and Target-ex.

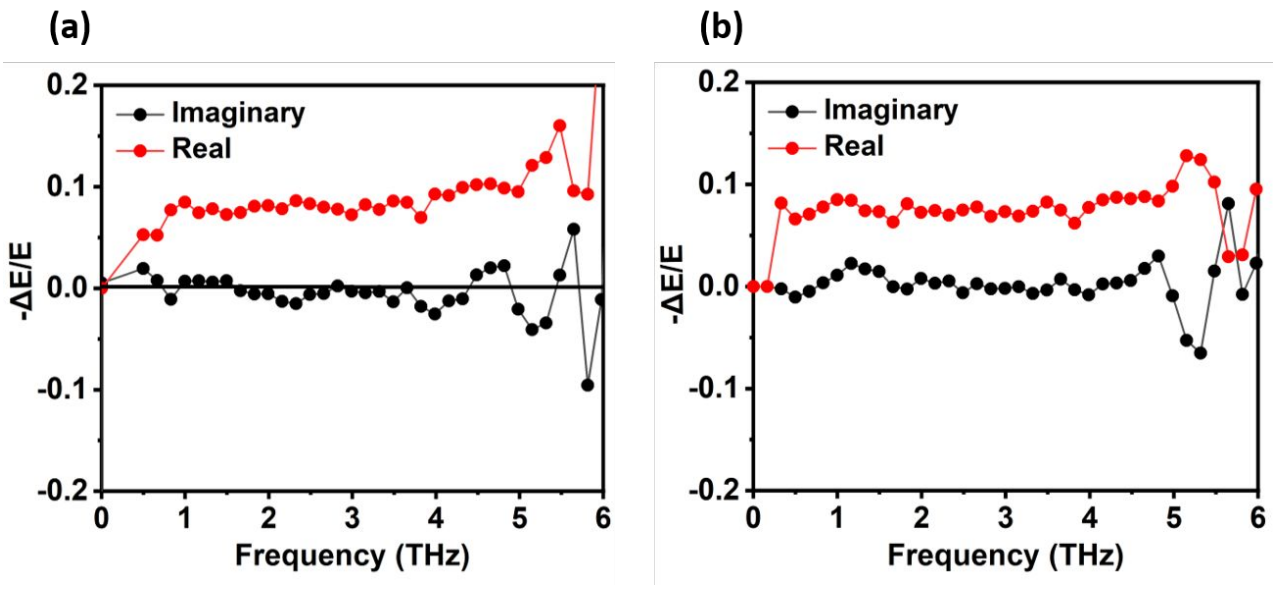

Figure S7. The spectra of TRTS for both the control (a) and Target (b).

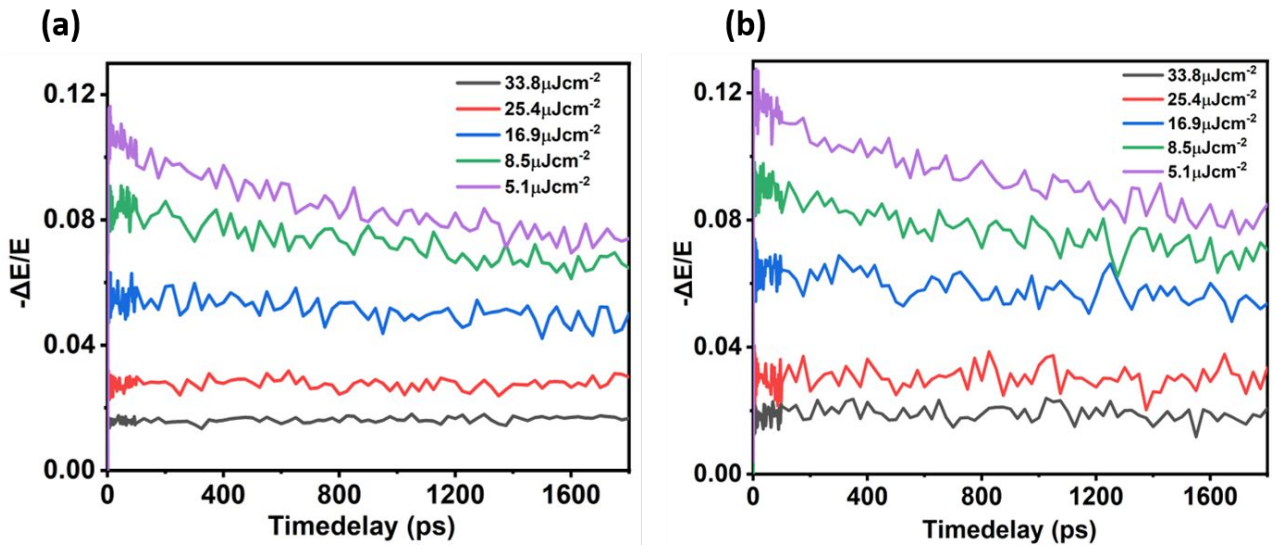

Figure S8. The spectra of TRTS for both the control (a) and Target (b) at different fluence.

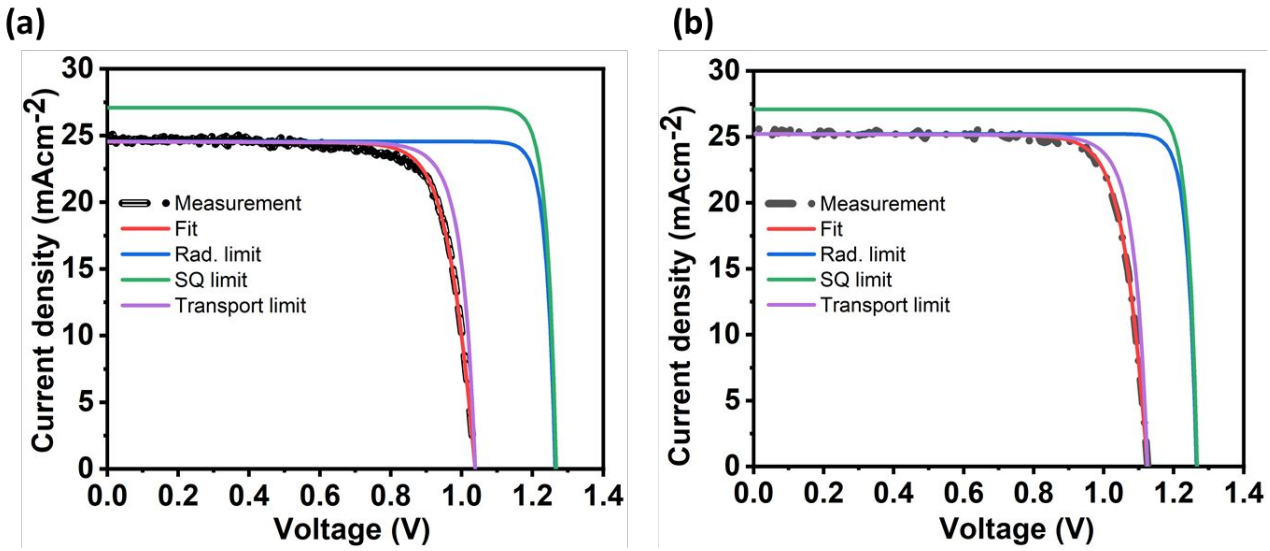

Figure S9. J-V curves of measured and simulated devices (a) Control and (b) Target.

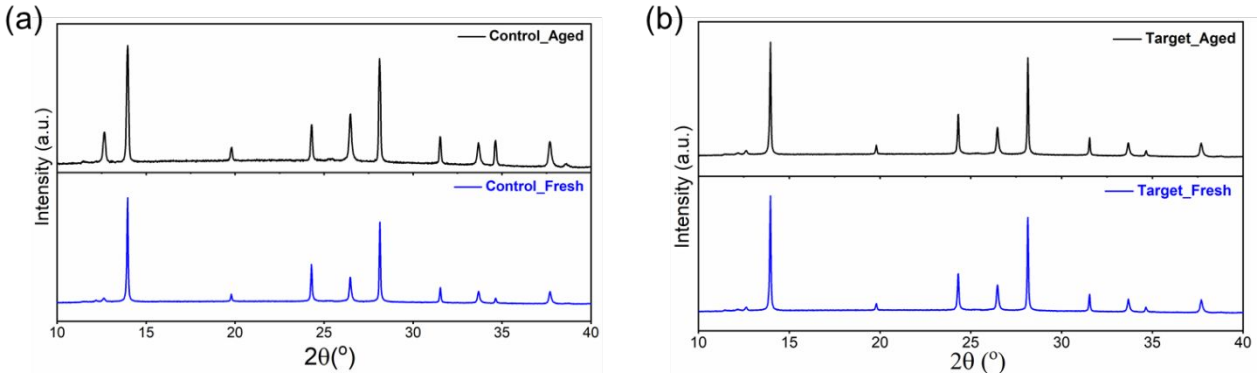

Figure S10. XRD of the (a) control and (b) target film before and after aging.

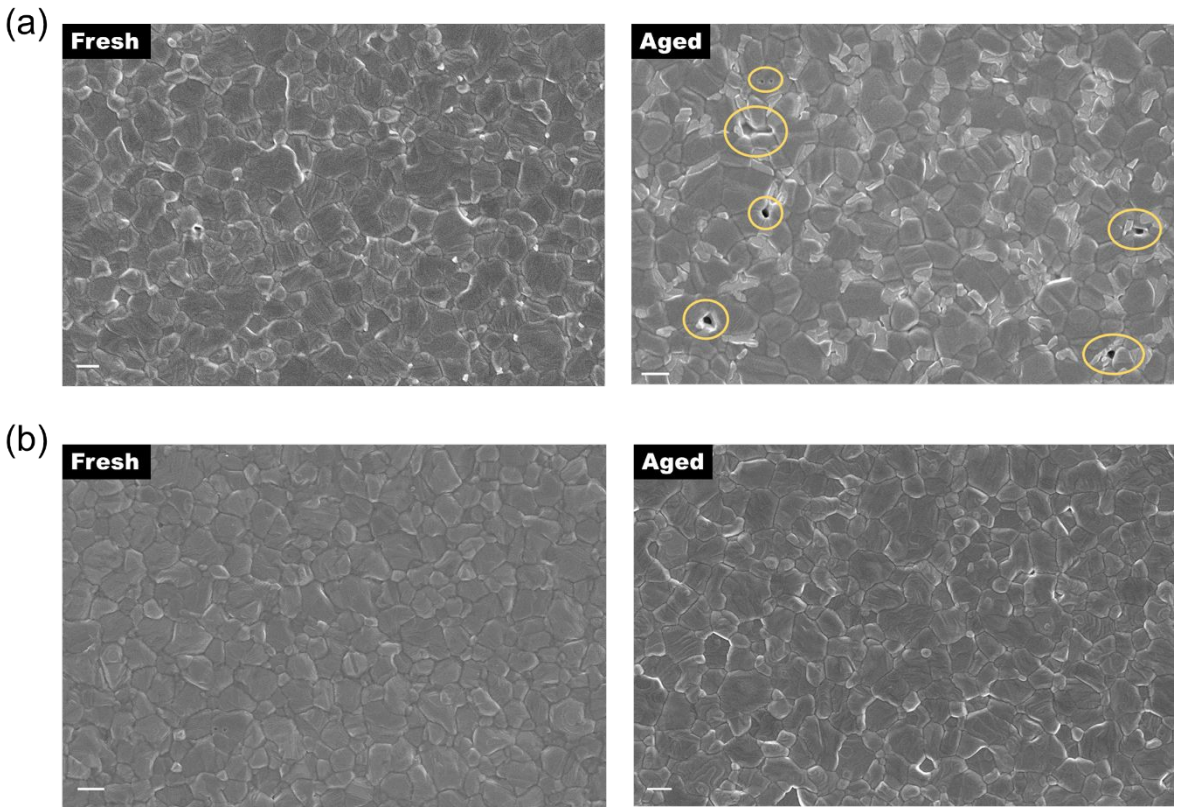

Figure S11. Top-view SEM images of the (a) control and (b) target film before and after aging. The scale bar is 1 μm.

Table S3. Bulk recombination: TRPL summarized results.

Condition	τ (ns)	$K1$(1/s)	L_D (um)
Control	2.65 e+02	1.95 e+06	0.721
Target 1	4.84 e+02	1.03 e+06	1.065
Target 2	2.74 e+02	1.83 e+06	0.779

Table S4. Surface recombination: TRPL summarized results.

Condition	S (cm/s)
Control	118
Target 1	62.3
Target 2	110

Note 1. Calculating the photoconductivity and mobility from TRTS measurements.

THz absorption is typically reported as – ΔE/E, where ΔE is the change in the modulus of the THz field after transmission through the sample and E is the modulus of the incident field. For thin films, where ΔE is typically much smaller than E, this ratio is proportional to the photoconductivity, which itself is proportional to the mobility[2].

Therefore, by using the following equations, we can calculate the photoconductivity and subsequently the mobility from the TRTS results.

The photoconductivity, Δσ, can be calculated using the following equation:

$$\Delta\sigma = \frac{-(n_{air}+n_{quartz})\varepsilon_0 c}{L} \cdot \frac{\Delta E}{E}$$

Where n_{air} and n_{quartz} are the refractive indices of air and quartz, respectively, ε_0 is the vacuum permittivity, c is the speed of light, L is the sample thickness, and ΔE/E is the THz absorption as measured using TRTS.

The photoconductivity can then be used to calculate the mobility, using the following equation:

$$\mu = \frac{\Delta\sigma}{N \cdot e}$$

Where e is the charge of an electron and N is the carrier density. The carrier density, N, is calculated using the following equation:

$$N = f_{abs} N_p \phi$$

Where f_{abs} is the absorptance, measured using an integrating sphere, at the excitation wavelength subtracting the absorptance at 850 nm, N_p is the average photon density on the sample volume and ϕ is the carrier generation yield, assumed to be equal to 2.

Note 2. Estimation of the redox reaction energy

A first rough estimate about the feasibility of the redox reaction between MAI_3 and defect sites in $FAPbI_3$ discussed in the main text can be obtained from:

$\Delta E = E^{lat}_{FAPbI_3} - E^{IP}_{Pb} - E^{diss}_{I_3} - E^{diss}_{I_2} - 2E^{EA}_{I}$ where

$E^{lat}_{FAPbI_3}$= -29.7 eV/cell is the lattice energy of $FAPbI_3$ taken from Ref. [3]

E^{IP}_{Pb}=E(Pb^{2+})-E(Pb^0) = 7.4eV + 15.0 eV = 22.4 eV[4] is the ionisation energy of lead

$E^{diss}_{I_3}$is the dissociation energy of I_3^- => I_2 +I^- = -1.3 eV[5]

$E^{diss}_{I_2}$= I_2 -> 2I(0) = 1.54 eV is the dissociation energy of a iodine dimer[6]

and

E^{EA}_{I}= E(I^-) - E(I^0) = -3.06eV is the electron affinity of iodine[7].

From this one obtains ΔE = -13.2 eV, i.e. the reaction is exothermic.

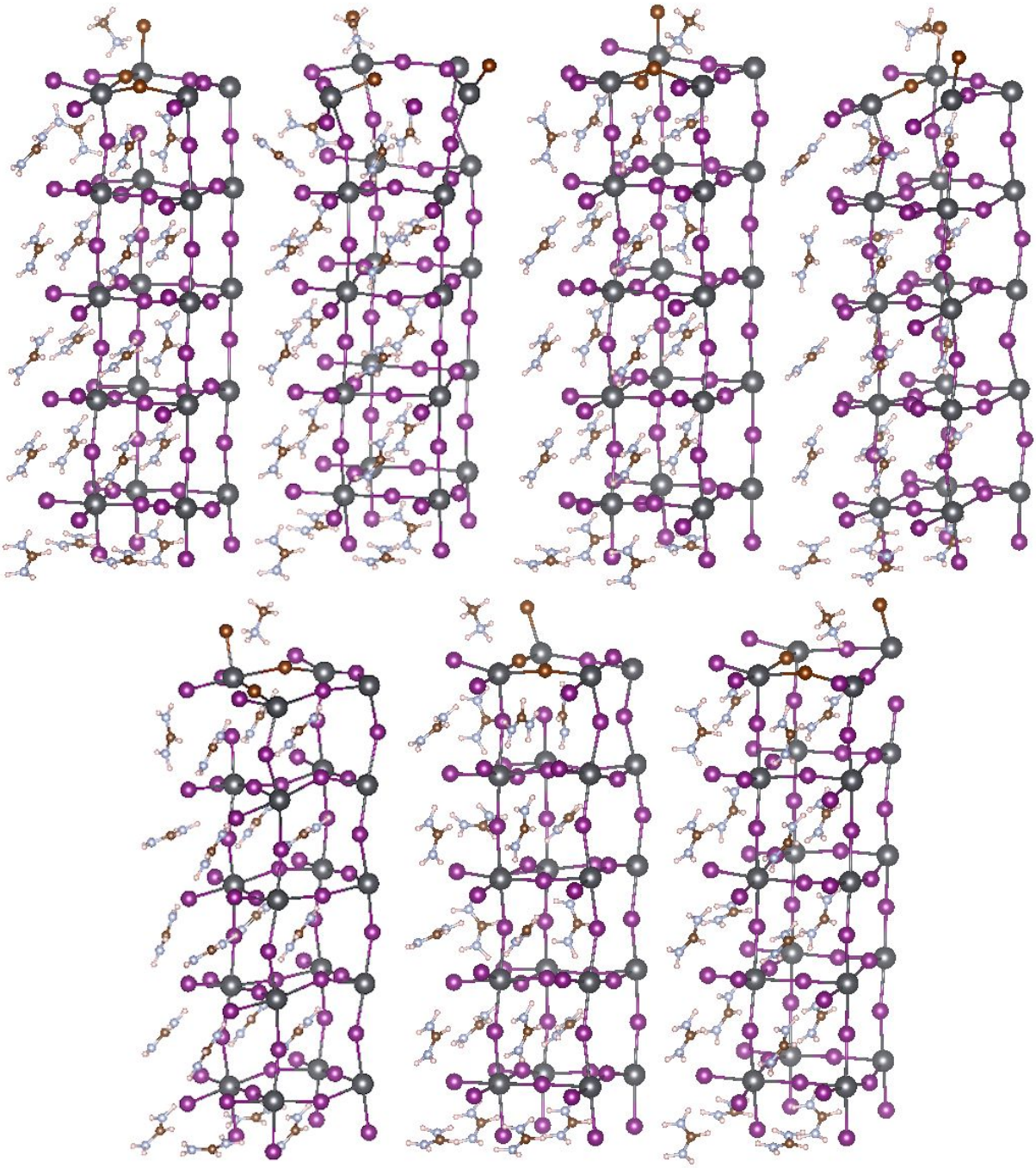

Figure S12: The seven obtained relaxed structures starting from different initial configuration of MAI_3 approaching a surface slab of $FAPbI_3$ with defects. The lowest energy structure is the bottom middle one and is used for the computation of the reaction energy and the Bader charges.

Table S3: Bader charges of the four lead atoms on the surface and the three-iodide atoms involved in the addition reaction of MAI_3 to $FAPbI_3$, showing that the I atoms originating from MAI_3 transfer in total a charge of 0.87e during the redox reaction.

	Pb#1	Pb#2	Pb#3	Pb#4	I#1	I#2	I#3
Initial State	**0.653**	**0.751**	**0.862**	**0.896**	**-0.438**	**-0.048**	**-0.298**
Final State	0.936	0.916	0.916	**0.917**	**-0.572**	**-0.516**	**-0.574**

Bibliography

(1) Mattoni, A.; Filippetti, A.; Saba, M. I.; Delugas, P. Methylammonium Rotational Dynamics in Lead Halide Perovskite by Classical Molecular Dynamics: The Role of Temperature. *J. Phys. Chem. C* **2015**, *119* (30), 17421–17428.

(2) *Terahertz Spectroscopy: Principles and Applications*, 1st ed.; Dexheimer, S. L., Ed.; CRC Press, 2008.

(3) Frost, J. M.; Butler, K. T.; Brivio, F.; Hendon, C. H.; Van Schilfgaarde, M.; Walsh, A. Atomistic Origins of High-Performance in Hybrid Halide Perovskite Solar Cells. *Nano Lett.* **2014**, *14* (5), 2584–2590.

(4) Lead (Pb) - Chemical properties, Health and Environmental effects.

(5) I3 anion. https://webbook.nist.gov/cgi/cbook.cgi?ID=B227&Mask=28F, (accessed 4 May 2021).

(6) Leroy, R. J. Molecular Constants and Internuclear Potential of Ground-State Molecular Iodine. *J. Chem. Phys.* **1970**, *52* (5), 2678–2682.

(7) Iodine atom, , https://webbook.nist.gov/cgi/cbook.cgi?ID=C14362448&Mask=20, (accessed 4 May 2021).